SPECIAL CAHMDA V COLLECTION

# Global Calibration of the GEOS-5 L-Band Microwave Radiative Transfer Model over Nonfrozen Land Using SMOS Observations

GABRIËLLE J. M. DE LANNOY

*NASA Goddard Space Flight Center, Greenbelt, Maryland, and Laboratory of Hydrology and Water Management, Ghent University, Ghent, Belgium*

ROLF H. REICHLE

*NASA Goddard Space Flight Center, Greenbelt, Maryland*

VALENTIJN R. N. PAUWELS*

*Laboratory of Hydrology and Water Management, Ghent University, Ghent, Belgium*

(Manuscript received 26 June 2012, in final form 28 November 2012)

ABSTRACT

A zero-order (tau-omega) microwave radiative transfer model (RTM) is coupled to the Goddard Earth Observing System, version 5 (GEOS-5) catchment land surface model in preparation for the future assimilation of global brightness temperatures (Tb) from the L-band (1.4 GHz) Soil Moisture Ocean Salinity (SMOS) and Soil Moisture Active Passive (SMAP) missions. Simulations using literature values for the RTM parameters result in Tb biases of 10–50 K against SMOS observations. Multiangular SMOS observations during nonfrozen conditions from 1 July 2011 to 1 July 2012 are used to calibrate parameters related to the microwave roughness $h$, vegetation opacity $\tau$ and/or scattering albedo $\omega$ separately for each observed 36-km land grid cell. A particle swarm optimization is used to minimize differences in the long-term (climatological) mean values and standard deviations between SMOS observations and simulations, without attempting to reduce the shorter-term (seasonal to daily) errors. After calibration, global Tb simulations for the validation year (1 July 2010 to 1 July 2011) are largely unbiased for multiple incidence angles and both H and V polarization [e.g., the global average absolute difference is 2.7 K for $Tb_H(42.5°)$, i.e., at 42.5° incidence angle]. The calibrated parameter values depend to some extent on the specific land surface conditions simulated by the GEOS-5 system and on the scale of the SMOS observations, but they also show realistic spatial distributions. Aggregating the calibrated parameter values by vegetation class prior to using them in the RTM maintains low global biases but increases local biases [e.g., the global average absolute difference is 7.1 K for $Tb_H(42.5°)$].

## 1. Introduction

Assimilating low-frequency (1–10 GHz) passive microwave observations into land surface models is expected to improve estimates of land surface conditions and, hence, weather and climate predictions. Global observations of brightness temperatures (Tb) are available from the (late) Advanced Microwave Scanning Radiometer–Earth Observing System (AMSR-E), the Soil Moisture Ocean Salinity (SMOS; Kerr et al. 2010) mission, and *Aquarius* (Le Vine et al. 2007). Soil moisture has a dominant effect on Tb at frequencies lower than ~10 GHz and lower incidence angles, whereas vegetation becomes more dominant at higher frequencies and higher incidence angles (Wigneron et al. 1993; Ferrazzoli et al. 1995). The lower-frequency observations (1.4 GHz) from SMOS and the future Soil Moisture Active Passive (SMAP; Entekhabi et al. 2010) mission are sensitive to

* Current affiliation: Department of Civil Engineering, Monash University, Clayton, Victoria, Australia.

*Corresponding author address:* Gabriëlle J. M. De Lannoy, NASA Goddard Space Flight Center, Code 610.1, Greenbelt Road, Greenbelt, MD 20771.
E-mail: gabrielle.delannoy@nasa.gov

DOI: 10.1175/JHM-D-12-092.1

© 2013 American Meteorological Society

greater depths into the surface and allow a soil moisture estimation with a reduced vegetation screening error compared to earlier missions (e.g., AMSR-E at 10.7 GHz). The benefit of using satellite soil moisture retrievals in large-scale data assimilation systems has been shown in multiple studies (Liu et al. 2011; Pan et al. 2012). However, only a few studies discussed the direct assimilation of satellite-based Tb at larger scales (Reichle et al. 2001; Balsamo et al. 2006). One of the reasons is the complexity of representing radiative transfer processes at the global scale, which will be addressed in this paper.

Successful use of satellite Tb observations in a soil moisture and soil temperature analysis system requires an accurate and unbiased model of the microwave radiative transfer processes. Examples of radiative transfer models (RTMs) include the Land Parameter Retrieval Model (LPRM; Owe et al. 2008), the Land Surface Microwave Emission Model (LSMEM; Drusch et al. 2001) and the L-band Microwave Emission of the Biosphere model (L-MEB; Wigneron et al. 2007). The Community Microwave Emission Modeling Platform (CMEM; Holmes et al. 2008; Drusch et al. 2009; de Rosnay et al. 2009) collects a variety of submodels within a single software framework. For the land surface emissivity alone, there is a wide variety of modules for the surface roughness, canopy layer, atmosphere, and dielectric mixing models. The parameters in these modules have typically been estimated using Tb observations from local field experiments, for example, using ground-based and airborne radiometers (de Rosnay et al. 2006; Grant et al. 2007; Jackson et al. 1999; Panciera et al. 2009b; de Jeu et al. 2009; Sabater et al. 2011; Montzka et al. 2013; Bircher et al. 2012). Zhang et al. (2012) calibrated their RTM for wetland conditions using AMSR-E Tb, and Fitzmaurice and Crow (2011) presented an online vegetation parameter estimation using synthetic Tb observations, all for small study areas. As we will show below, using locally determined microwave RTM parameters in a global modeling system can lead to strongly biased Tb estimates. Large-scale studies on the parameterization of RTMs and the assessment of effective parameters using satellite data have been limited (Drusch et al. 2009; de Rosnay et al. 2009).

In preparation for the global assimilation of Tb from SMOS and SMAP, a zero-order (tau-omega) microwave RTM is coupled here to the Goddard Earth Observing System, version 5 (GEOS-5) catchment land surface model (CLSM; Koster et al. 2000). We calibrate select RTM parameters using multiangular H- and V-polarized SMOS observations to obtain climatologically unbiased Tb from the modeling system. The calibration is designed to mitigate long-term biases. Short-term random errors and (seasonal) biases can be accounted for within the data assimilation system (De Lannoy et al. 2007; Reichle et al. 2010). Ultimately, the calibrated modeling system developed here will facilitate Tb assimilation to improve global estimates of surface and root zone soil moisture, soil temperature, and vegetation state variables (Wigneron et al. 2002) and support the generation of the SMAP Level 4 Surface and Root Zone Soil Moisture (L4_SM) product (Reichle et al. 2012).

## 2. Data and models

### a. SMOS observations and preprocessing

Since its launch in November 2009, the SMOS mission provides global Tb observations at a nominal spatial resolution of 43 km and with a local overpass every 3 days at the equator. L-MEB is used operationally by the SMOS mission to retrieve surface soil moisture and vegetation opacity $\tau$ from the Tb measurements (Wigneron et al. 2007). For this study, we use observations from the period 1 January 2010 to 1 October 2012. Specifically, we use the multiangular full-polarization Tb fields (MIR_SCLF1C) to calibrate the RTM and the retrieved soil moisture and $\tau$ fields (MIR_SMUDP2) for comparison against CLSM soil moisture and calibrated $\tau$ values. We use reprocessed data (processing versions SCLF1C 504 and SMUDP2 501) for the years 2010 and 2011. For 2012, we use the daily updated data (processing versions SCLF1C 504 and 505 and SMUDP2 500 and 551) distributed by the European Space Agency.

The preprocessing of the SMOS observations for use in the present study involves several steps. First, we collect all antenna-level SMOS SCLF1C Tb observations for a given grid cell and half orbit. We then apply a quality control to their angular signature by eliminating observations that fall outside of a one-standard-deviation range around the 5° angular moving average (done separately for each half orbit and grid cell). Thereafter, we transform (geometric and Faraday rotation) the SMOS SCLF1C Tb data from the antenna reference frame to the top of the atmosphere using information provided with the observations (CESBIO et al. 2011; http://www.cesbio.ups-tlse.fr/SMOS_blog/wp-content/uploads/TOOLS/XY2HV.m). After the rotation, the observations are binned per 1° incidence angle. For this paper, only a subset of all processed angles is used: $\theta$ = 32.5°, 37.5°, 42.5°, 47.5°, 52.5°, and 57.5°, where, for example, 32.5° represents the average of all observations with incidence angles between 32° and 33°. Incidence angles below 20° have shown some unresolved deviation from the expected angular signature (Martín-Neira et al. 2012) and were therefore excluded. We further apply

a strict quality control by eliminating observations that are (i) obviously contaminated by radio frequency interference (RFI), that is, Tb > 320 K or according to the RFI flags in the SMOS products; (ii) near water bodies; or (iii) outside of the sensor footprint's alias-free zone. Next, both the SCLF1C Tb and SMUDP2 soil moisture are aggregated from the 15-km discrete global grid (DGG) on which they are posted to the 36-km Equal-Area Scalable Earth Grid (EASE) that will be used for SMAP Tb observations. The aggregation is a simple spatial averaging of all the DGG cells with centers inside an EASE grid cell and performed for each incidence angle and polarization independently. During this aggregation step, the data are screened for excessive sub-36-km heterogeneity that may be indicative of RFI or the presence of open water bodies. Specifically, we retain only aggregated soil moisture retrievals that have a maximum standard deviation of 0.2 $m^3\ m^{-3}$ in the 15-km retrievals within a 36-km grid cell. Similarly, Tb observations are retained only if the sub-36-km standard deviation is less than 7 K. Also, we require that at least two 15-km observations are included in the 36-km aggregate. The final quality check involves the elimination of data taken (i) during intensive rain events (precipitation > 10 mm $h^{-1}$), (ii) near or below freezing conditions (temperature < 273.4 K), or (iii) when snow is present (snow water equivalent > $10^{-4}$ kg $m^{-2}$) based on GEOS-5 estimates of temperature, precipitation, and snow. Furthermore, only soil moisture observations with an average retrieval uncertainty (provided with the SMUDP2 product) less than 0.2 $m^3\ m^{-3}$ are selected. The above quality standards are based on our best judgment, through trial and error and inspection of the retained data.

### b. GEOS-5 catchment land surface model

The GEOS-5 CLSM has many of the features found in other land surface models used with climate models, including subsurface soil moisture and heat transport, a multilayer snow scheme, and complete energy and water balance equations for each of several heat and moisture reservoirs. Unique to the CLSM is its use of subgrid-scale topographic data to model explicitly the horizontal variability of soil moisture within a given surface element, which leads to conceptually improved treatments of subsurface moisture dynamics, evaporation, and runoff (Koster et al. 2000).

For this study CLSM is set up on the 36-km SMAP EASE grid and spun up for 18 years prior to the SMOS observation period using surface meteorological forcing data at ½° × ⅔° spatial and hourly temporal resolution from the Modern-Era Retrospective Analysis for Research and Applications (MERRA; Rienecker et al. 2011). The MERRA precipitation is corrected with the National Oceanic and Atmospheric Administration (NOAA) Climate Prediction Center unified gauge-based precipitation product (Reichle 2012). The CLSM model version used here is the same as that used in GEOS-5.7.2, which is also used for the MERRA-Land data product (Reichle et al. 2011), except for two changes that align the model more closely with the version that will ultimately be used for the SMAP L4_SM data product: (i) the surface soil moisture is diagnosed for the top-5-cm surface layer (as opposed to the top-2-cm layer used in GEOS-5.7.2) and (ii) the model is used here with a preliminary version of updated soil parameters from a forthcoming version of GEOS-5.

The new soil texture is a composite of different data sources, including the Food and Agricultural Organization (FAO) dataset, Harmonized World Soil Database (HWSD), State Soil Geographic (STATSGO), Australian Soil Resources Information System (ASRIS), and National Soil Database Canada (NSDC). Furthermore, the texture is stratified by low, medium, and high organic material. For each texture class, a unique set of soil hydraulic parameters is derived using the pedotransfer functions of Wösten et al. (2001). The wilting point is determined through an inversion of the corresponding Campbell (1974) tension curve at −1500 kPa. Collectively, these changes alter the soil moisture climatology compared to that of the original GEOS-5.7.2 version for better agreement with in situ observations (see appendix A).

The CLSM has eight vegetation classes, and the vegetation processes are parameterized by spatially distributed climatological vegetation information, including Advanced Very High Resolution Radiometer (AVHRR)-based monthly leaf area index (LAI) and greenness. For the application of the RTM only, we further subsample the 8 vegetation classes into the 16 classes defined by the Moderate Resolution Imaging Spectroradiometer (MODIS; 500 m MOD12Q1V004) International Geosphere–Biosphere Programme (IGBP) land cover classification. At the 36-km EASE resolution, each grid cell is assigned a single dominant IGBP-vegetation type, thereby neglecting subpixel heterogeneity.

### c. L-band radiative transfer model

A zero-order tau-omega microwave RTM is coupled here to the GEOS-5 CLSM that converts soil moisture, soil temperature, vegetation water content, and air temperature into L-band Tb estimates at the top of the atmosphere [$Tb_{TOA,p}$ (K)] at polarization $p = (H, V)$ (horizontal or vertical) as follows:

$$\mathrm{Tb}_{\mathrm{TOV},p} = T_s(1-r_p)A_p + T_c(1-\omega_p)(1-A_p)(1+r_pA_p) + \mathrm{Tb}_{\mathrm{ad},p}r_pA_p^2, \quad (1)$$

$$\mathrm{Tb}_{\mathrm{TOA},p} = \mathrm{Tb}_{\mathrm{au},p} + \exp(-\tau_{\mathrm{atm},p})\mathrm{Tb}_{\mathrm{TOV},p}, \quad (2)$$

where $\mathrm{Tb}_{\mathrm{TOA},p}$ (K) is the top of vegetation Tb, $T_s$ (K) is the surface soil temperature, $T_c$ (K) is the canopy temperature (assumed equal to $T_s$), $\mathrm{Tb}_{\mathrm{ad},p}$ (K) and $\mathrm{Tb}_{\mathrm{au},p}$ (K) are the downward and upward atmospheric radiation, $A_p$ (–) is the vegetation attenuation, $\exp(-\tau_{\mathrm{atm},p})$ (–) is the atmospheric attenuation, $\tau_{\mathrm{atm},p}$ (–) is the atmospheric optical depth, $r_p$ (–) is the rough surface reflectivity, and $\omega_p$ (–) is the scattering albedo. The atmospheric contributions [$\mathrm{Tb}_{\mathrm{ad},p}$, $\mathrm{Tb}_{\mathrm{au},p}$, and $\exp(-\tau_{\mathrm{atm},p})$] are described by Pellarin et al. (2003). The rough surface reflectivity $r_p$ (–) is derived from the smooth surface reflectivity $R_p$ (–) following Choudhury et al. (1979) and Wang and Choudhury (1981):

$$r_p = [QR_q + (1-Q)R_p]\exp(-h)\cos^{\mathrm{Nr}_p}(\theta), \quad (3)$$

where $Q$ (–) is the polarization mixing ratio, $\theta$ (rad) is the incidence angle, $h$ (–) is the roughness parameter accounting for dielectric properties that vary at the subwavelength scale, $\mathrm{Nr}_p$ (–) is the angular dependence, and $q = V$ for $p = H$ and vice versa. Polarization coupling effects are small at L-band frequencies (Kerr and Njoku 1990), and we therefore set $Q \equiv 0$. The smooth surface reflectivity $R_p$ (–) is given by the Fresnel equations as a function of the dielectric constant, which itself depends on soil moisture, temperature, texture, incidence angle, and wavelength. We select the Wang and Schmugge (1980) soil dielectric mixing model for this study. The results with this model are similar to what is obtained with the Mironov et al. (2004) model, and both are in a better agreement with the SMOS data than the Dobson et al. (1985) model (consistent with de Rosnay et al. 2009).

Equation (1) reflects that Tb is less sensitive to soil moisture in areas with substantial vegetation, because the water within the vegetation attenuates the emission from the soil and adds its own emission contribution. The presence of litter (dead plant material) typically increases emissions, especially when wet (Grant et al. 2007). In addition, rainwater intercepted by the vegetation absorbs microwave radiation and thereby also masks emission from the soil (Saleh et al. 2006). However, litter and interception effects are neglected here. The vegetation attenuation $A_p$ (–) is based on the Jackson and Schmugge (1991) vegetation opacity model:

$$A_p = \exp\left(-\frac{\tau_p}{\cos\theta}\right), \quad \text{with} \quad (4)$$

$$\tau_p = b_p\mathrm{VWC} = b_p\mathrm{LEWTLAI}, \quad (5)$$

where $\tau_p$ (–) is the nadir vegetation opacity, which is a function of a vegetation structure parameter $b_p$ (–) and the vegetation water content (VWC; kg m$^{-2}$). The latter is modeled here as the product of LAI (m$^2$ m$^{-2}$) and the leaf equivalent water thickness (LEWT; kg m$^{-2}$).

In summary, the key parameters for the rough surface reflectivity [Eq. (3)], the scattering albedo, and vegetation optical depth [Eq. (5)] will be calibrated using multiangular SMOS observations, as outlined in section 3. We use the default empirical expressions for the remaining submodels of the dielectric constant (Wang and Schmugge 1980) and the atmospheric optical depth (Pellarin et al. 2003).

A variety of parameterizations and parameter values exists for microwave soil roughness and vegetation effects. A direct comparison of literature values for RTM parameters is not straightforward because they are estimated with slightly different models for various purposes (mostly soil moisture retrieval, rather than forward Tb modeling) and are primarily based on local experiments. For this paper, we assembled three different sets of parameter values from the literature:

(i) Lit1 values are based on look-up tables suggested for the future SMAP L2/3_SM_P product (radiometer soil moisture retrieval) (O'Neill et al. 2012), which are largely inherited from an earlier Hydros Observing System Simulation Experiment by Crow et al. (2005), except for the LEWT (see below);
(ii) Lit2 values are collected from studies that use L-MEB, LSMEM and CMEM (Drusch et al. 2009; de Rosnay et al. 2009; Grant et al. 2008; Wigneron et al. 2007; Saleh et al. 2007); and
(iii) Lit3 is similar to Lit2, but with $\mathrm{Nr}_p = 0$ and with the soil roughness $h$ as used in SMOS Tb monitoring with CMEM (Sabater et al. 2011) at the European Centre for Medium-Range Weather Forecasts (ECMWF).

These three sets of literature values are used in two ways. First, we simulate Tb using the literature values for the microwave RTM parameters and compare the results against SMOS observations. Second, the literature values are used as prior constraints in the parameter calibration (section 3). Table 1 shows the most relevant RTM parameter values for L-band wavelengths for the three sets of literature values broken down by the applicable IGBP vegetation classes. Details of the parameterizations of microwave soil roughness $h$, vegetation opacity $\tau$, and scattering albedo $\omega$ are discussed in appendix B. As can be seen in Table 1, microwave soil roughness parameter

TABLE 1. Literature-based microwave RTM parameters ($Nr_H = Nr_V = 0$ for Lit1 and Lit3).

| IGBP land cover class | $h = h_{min} = h_{max}$ (–) | | | $Nr_H$ (–) | $Nr_V$ (–) | $\omega$ (–) | | LEWT (kg m$^{-2}$) | | $b_H = b_V$ (–) | |
|---|---|---|---|---|---|---|---|---|---|---|---|
| | Lit1 | Lit2 | Lit3 | Lit2 | Lit2 | Lit1 | Lit2, Lit3 | Lit1 | Lit2, Lit3 | Lit1 | Lit2, Lit3 |
| 1 ENF Evergreen needleleaf forest | 0.16 | 1.2 | 1.66 | 1 | 0 | 0.12 | 0.05 | 0.3 | 1 | 0.1 | 0.33 |
| 2 EBF Evergreen broadleaf forest | 0.16 | 1.3 | 1.66 | 1.75 | 0 | 0.12 | 0.05 | 0.3 | 1 | 0.1 | 0.33 |
| 3 DNF Deciduous needleleaf forest | 0.16 | 1.2 | 1.66 | 1 | 0 | 0.12 | 0.05 | 0.2 | 1 | 0.12 | 0.33 |
| 4 DBF Deciduous broadleaf forest | 0.16 | 1 | 1.66 | 1 | 2 | 0.12 | 0.05 | 0.2 | 1 | 0.12 | 0.33 |
| 5 MXF Mixed forest | 0.16 | 1.3 | 1.66 | 1 | 1 | 0.08 | 0.05 | 0.2 | 1 | 0.12 | 0.33 |
| 6 CSH Closed shrublands | 0.11 | 0.7 | 1.66 | 1 | 0 | 0.05 | 0.05 | 0.2 | 0.5 | 0.11 | 0.3 |
| 7 OSH Open shrublands | 0.11 | 0.7 | 1.66 | 1 | 0 | 0.05 | 0.05 | 0.2 | 0.5 | 0.11 | 0.3 |
| 8 WSV Woody savannas | 0.125 | 0.7 | 1.66 | 1 | 0 | 0.12 | 0.05 | 0.15 | 0.5 | 0.11 | 0.3 |
| 9 SAV Savannas | 0.156 | 0.5 | 1.66 | 1 | 0 | 0.08 | 0.05 | 0.15 | 0.5 | 0.11 | 0.2 |
| 10 GRS Grasslands | 0.156 | 0.1 | 1.66 | 1 | 0 | 0.05 | 0.05 | 0.15 | 0.5 | 0.1 | 0.2 |
| 12 CRP Croplands | 0.108 | 0.5 | 1.66 | 0 | −1 | 0.05 | 0.05 | 0.15 | 0.5 | 0.11 | 0.15 |
| 14 CRN Cropland and natural vegetation | 0.13 | 0.7 | 1.66 | 0 | −1 | 0.065 | 0.05 | 0.15 | 0.5 | 0.11 | 0.15 |
| 16 BAR Barren or sparsely vegetated | 0.15 | 0.1 | 1.66 | 0 | −1 | 0 | 0.05 | 0 | 0 | 0 | 0 |

values for $h$ and $Nr_p$ differ greatly across the three sets of literature values. For the parameter calibration, we assume that $h$ depends on soil moisture and varies between $h_{min}$ and $h_{max}$ (see appendix B for details). The higher $h$ and higher $Nr_p$ in Lit2 and Lit3 result in higher Tb with lower variability than Lit1. Table 1 further shows the vegetation parameters LEWT and $b_p$ that directly affect the vegetation opacity [Eq. (5)]. The LEWT and $b_p$ are substantially smaller for Lit1 than for Lit2 and Lit3. The lower opacity for Lit1 limits the contribution of vegetation to Tb values (mostly resulting in a lower Tb), but assures a high sensitivity to soil contributions. For the calibration, $b_p$ is assumed to depend on polarization. Finally, the Lit1 and Lit2 or Lit3 values for the scattering albedo ($\omega$) differ somewhat (Table 1). Less scattering leads to higher Tb. For the calibration, $\omega$ is assumed to be independent of polarization. Note that after calibration we obtain an "effective" $h$ that no longer just represents subwavelength-scale dielectric roughness. Likewise, we obtain effective values for $\tau$ and $\omega$ that no longer reflect the assumption of single scattering (Kurum et al. 2012).

## 3. Calibration

In section 4, it will be shown that the literature-based lookup table values for the microwave RTM result in considerable biases of the simulated GEOS-5 Tb compared to SMOS observations. Through parameter calibration we therefore minimize the *climatological* differences between the simulated and SMOS-observed Tb, without attempting to reduce the shorter-term errors that can be dealt with through Tb data assimilation. The RTM parameters are optimized locally, that is, for each grid cell independently, and for the land surface conditions simulated by the GEOS-5 modeling system.

### a. Objective function

The particle swarm optimization (PSO; Kennedy and Eberhart 1995) search algorithm is used to maximize the Gaussian likelihood of a microwave RTM parameter set, given a set of multiangular SMOS Tb observations. A prior random set of parameter vectors (or particles; $\alpha$) iteratively explores the search space. At each iteration, the velocity (speed and direction) of each particle is adjusted based on the most favorable conditions that have been experienced by the individual particle (cognitive aspect) and the swarm as a whole (social aspect). The iterative swarm search is performed in several independent repetitions to mitigate sampling limitations. Details and examples of hydrological studies using this algorithm can be found, for example, in Scheerlinck et al. (2009) and Pauwels and De Lannoy (2012). The PSO parameters are further discussed in section 3b.

To maximize the posterior likelihood, we minimize the objective function $J$ (–), which contains penalty terms for long-term bias in the Tb mean [$J_{\langle\cdot\rangle,o}$ (–)] and variability [$J_{s[\cdot],o}$ (–)] and a parameter penalty term [$J_\alpha$ (–)]:

$$J = W_m \sum_\theta \sum_p^{H,V} \sum_d^{A,D} \frac{N_{\theta,p,d}}{N} \frac{[\langle \mathrm{Tb}_o \rangle - \langle \mathrm{Tb}(\alpha) \rangle]^2_{\theta,p,d}}{\sigma_m^2} \Bigg\} J_{\langle\cdot\rangle,o} + W_s \sum_\theta \sum_p^{H,V} \sum_d^{A,D} \frac{N_{\theta,p,d}}{N} \frac{\{s[\mathrm{Tb}_o] - s[\mathrm{Tb}(\alpha)]\}^2_{\theta,p,d}}{\sigma_s^2} \Bigg\} J_{s[\cdot],o} + W_\alpha \frac{1}{N_\alpha} \sum_{i=1}^{N_\alpha} \frac{(\alpha_{0,i} - \alpha_i)^2}{\sigma^2_{\alpha_{0,i}}} \Bigg\} J_\alpha . \quad (6)$$

We minimize the difference between the observed $\mathrm{Tb}_o$ and the modeled $\mathrm{Tb}(\alpha)$ in the time series mean ($\langle\cdot\rangle$) and

variability ($s[\cdot]$, temporal standard deviation) with a target accuracy of $\sigma_m = 1$ K and $\sigma_s = 1$ K, respectively. Note that we do not minimize the difference between the simulations and observations at each individual time step in a root-mean-square sense. Instead, we minimize the difference between temporal means for each individual combination of polarization ($p = H, V$), ascending (0600 LT) or descending (1800 LT) orbit direction [$d = (A, D)$], and incidence angle ($\theta = 32.5°$, 37.5°, 42.5°, 47.5°, 52.5°, and 57.5°). The number of data points in time for a particular combination of angle, polarization, and orbit direction is represented by $N_{\theta,p,d}$ and $N$ is the total number of data points in time over all considered angles, polarizations, and orbit directions.

We also limit the deviation of each calibrated parameter ($\alpha_i$) from a vegetation-dependent prior constraint $\alpha_{0,i}$ with a standard deviation of $\sigma_{\alpha_{0,i}}$. The latter is given by $\sigma^2_{\alpha_{0,i}} = (\alpha_{\max,i} - \alpha_{\min,i})^2/12$, which is the variance of a uniform distribution with boundaries ($\alpha_{\max,i}$, $\alpha_{\min,i}$); $N_\alpha$ is the number of simultaneously calibrated parameters and varies between 2 and 5 (see section 3b). The parameter penalty can be seen as a regularization term to effectively select one "best" parameter set among the multiple parameter sets that could be consistent with the observations (equifinality); $W_m = 2$, $W_s = 2$, and $W_\alpha = 3$ are weight factors for the different penalty terms and are meant to balance the constraining effect of each term. As will be shown below (section 4), $J_{\langle\cdot\rangle,o}$ is the largest component, that is, the biases in the mean values are much larger than the biases in the standard deviations. By giving $J_{\langle\cdot\rangle,o}$ and $J_{s[\cdot],o}$ equal weights, we effectively emphasize the need for unbiased Tb simulations in the mean, and $J_{s[\cdot],o}$ is of secondary importance. The parameter penalty term is generally the smallest and is less constraining than the other terms despite its greater weight factor.

### b. Calibration details

A number of assumptions in the calibration setup affect the optimized parameter estimates, including the specific set of parameters selected for calibration, the prior parameter constraints ($\alpha_0$), the allowable range of parameter values ($\alpha_{\min}$, $\alpha_{\max}$), their prior standard deviation ($\sigma_{\alpha_0}$), the weights ($W$) of each of the three penalty terms, the length of the time series, the selected incidence angles (number of constraining observations), and the PSO parameters. The parameters that are never calibrated in this exercise are $Q = 0$, $\mathrm{Nr}_p$, and LEWT. The latter two parameters are indirectly compensated for through calibration of $h$ and $b_p$, respectively. The candidate RTM parameters for calibration are $h_{\min}$, $\Delta h$, $b_H$, $\Delta b$, and $\omega$, where $\Delta h \equiv h_{\max} - h_{\min}$ and $\Delta b \equiv b_V - b_H$. Table 2 lists the four different subsets of these parameters (labeled A, B, C, and D) that are calibrated in different experiments. Because the climatological mean Tb is highly sensitive to the microwave roughness, the parameters $h_{\min}$ and $\Delta h$ are included in all calibration scenarios. The four scenarios thus combine the calibration of $h_{\min}$ and $\Delta h$ with the calibration of neither, either, or both the scattering albedo $\omega$ and vegetation structure parameters ($b_H$, $\Delta b$). In all scenarios, the selected parameters are calibrated simultaneously. Table 2 also shows the allowable range ($\alpha_{\min}$, $\alpha_{\max}$) of each calibrated parameter, based on values reported in the references cited above. This range is fixed for all scenarios and vegetation classes.

TABLE 2. RTM parameters selected for different calibration scenarios, with indication of the allowed parameter range.

| Parameter | (Min, max) | Scenario A | B | C | D |
|---|---|---|---|---|---|
| $h_{\min}$ | (0, 2.0) | X | X | X | X |
| $\Delta h \equiv h_{\max} - h_{\min}$ | (0, 1.0) | X | X | X | X |
| $\omega$ | (0, 0.3) | | X | | X |
| $b_H$ | (0, 0.7) | | | X | X |
| $\Delta b \equiv b_V - b_H$ | (−0.15, 0.15) | | | X | X |

The RTM parameters are constrained by prior values ($\alpha_0$) that depend on the vegetation class using the three sets of literature values listed in Table 1. Altogether, we repeat the calibration exercise 12 times, once for each of the four subsets of calibrated parameters (A, B, C, and D) with each of the three sets of prior constraints (Lit1, Lit2, and Lit3). For example, experiments CalA1, CalB1, CalC1, and CalD1 refer to the four calibration scenarios A, B, C, and D constrained by prior values based on Lit1 parameters. Experiments CalA1, CalA2, and CalA3 use the same set of calibrated parameters (i.e., $h_{\min}$ and $\Delta h$ for case A), but with prior constraints from Lit1, Lit2, and Lit3, respectively.

Parameters that are not calibrated in a particular scenario are set to their default literature values (Table 1). When calibrated, $\Delta h$ is subject to the constraint $\Delta h \geq 0$ and $\Delta b$ is confined to a relatively narrow range (Table 2). While $b_H < b_V$ in Crow et al. (2005) and O'Neill et al. (2012), there are also reports of $\tau_H > \tau_V$ (Wigneron et al. 2007). Therefore, we allow $\Delta b$ to assume either sign, while imposing the constraint that $b_V \geq 0$. For $\omega_p$, we calibrate a single polarization-independent value, because the literature shows little evidence of differences in $H$- and $V$-polarized $\omega$.

The soil-texture-dependent parameters (e.g., porosity and wilting point) also strongly affect the Tb estimates through their impact on the dielectric constant (Wang and Schmugge 1980) and the roughness model [Eq. (B1)].

However, we choose not to calibrate such CLSM parameters to assure consistency with the soil moisture and temperature values in the quasi-operational GEOS-5 system that is used for reanalysis data products, numerical weather prediction, and seasonal climate forecasting.

The initial values of the calibrated parameters (initial particle swarm) are uniformly distributed over each parameter's allowable range (Table 2). A particle swarm size of 25 is chosen and three repetitions are used. The initial and final PSO inertia weights are $w_0 = 0.9$ and $w_t = 0.7$, the cognitive and social parameters are $c_1 = 0.7$ and $c_2 = 1.3$, and the velocity factor is $\delta = 0.6$. These PSO parameter choices are not themselves optimized but (i) are selected within a range that should assure convergence (Trelea 2003) and (ii) impose a stronger social than cognitive impact on the particle velocity update ($c_2 > c_1$). We further enforce a minimum of 4 and a maximum of 30 iterations in each of the three repetitions and use a stop criterion when the objective function reaches a steady minimum, that is, when at least three iterations yield near-identical $J$ values (i.e., $|J_{i-3} - J_i| < 0.001$ for iteration $i$).

We split two years of SMOS data into a calibration period (1 July 2011 to 1 July 2012) and a validation period (1 July 2010 to 1 July 2011). The actual number of available SMOS observations strongly depends on the location. For example, the number of observations used during the calibration and validation periods is limited by RFI in Europe and Asia and by frozen conditions in northern latitudes or at high elevations. For both the calibration and validation statistics, we require a minimum of 20 data points per year for each combination of angle, polarization, and orbit direction, that is, $N_{\theta,p,d} \geq 20$ at a single location to assure some minimal sampling of the climatological temporal variability. The calibration involves 24 combinations of angles, polarizations, and orbits, so that the minimum total number of data points at each calibrated location is $N \geq 480$.

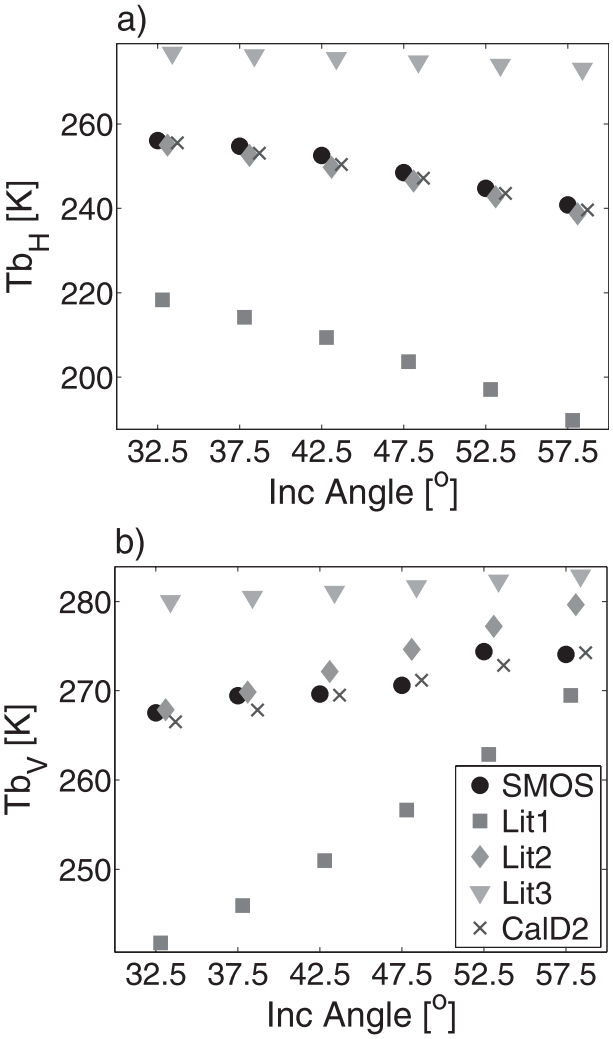


FIG. 1. Global annual mean values of ascending multiangular Tb from SMOS and simulations using different RTM parameter sets for (a) H and (b) V polarization during the validation period (1 Jul 2010 to 1 Jul 2011). Symbols are slightly offset from the nominal incidence angle for clarity.

## 4. Results

### a. Brightness temperature evaluation

#### 1) BEFORE CALIBRATION

Figure 1 shows SMOS and simulated Tb for the six incidence angles, averaged from 1 July 2010 to 1 July 2011 (validation period) and across the globe. With increasing incidence angle, H-polarized Tb decreases and V-polarized Tb increases. The Lit1 setup, however, is too cold by up to 50 K for H polarization and by up to 30 K for V polarization. The Lit1 Tb estimates also exhibit too much angular sensitivity. In contrast, the Lit3 setup is too warm by up to 30 K for H polarization and by up to 15 K for V polarization. Lit3 estimates also have insufficient angular sensitivity. The Lit2 setup is closest to the SMOS observations in terms of the global, annual mean.

Figures 2a and 2b show maps of the time series mean and standard deviation of SMOS $Tb_H$ at 42.5° incidence angle for the year 1 July 2010 to 1 July 2011. Substantial areas across Asia and Europe are screened out because of severe RFI contamination. The global average $Tb_H(42.5°)$ (excluding RFI-contaminated and predominantly frozen areas) for the validation year is 254.1 K, with a global average of 11.2 K for the $Tb_H(42.5°)$ time series standard deviation. The corresponding values for the calibration year (not shown) are 254.1 K and 10.9 K for the mean and standard

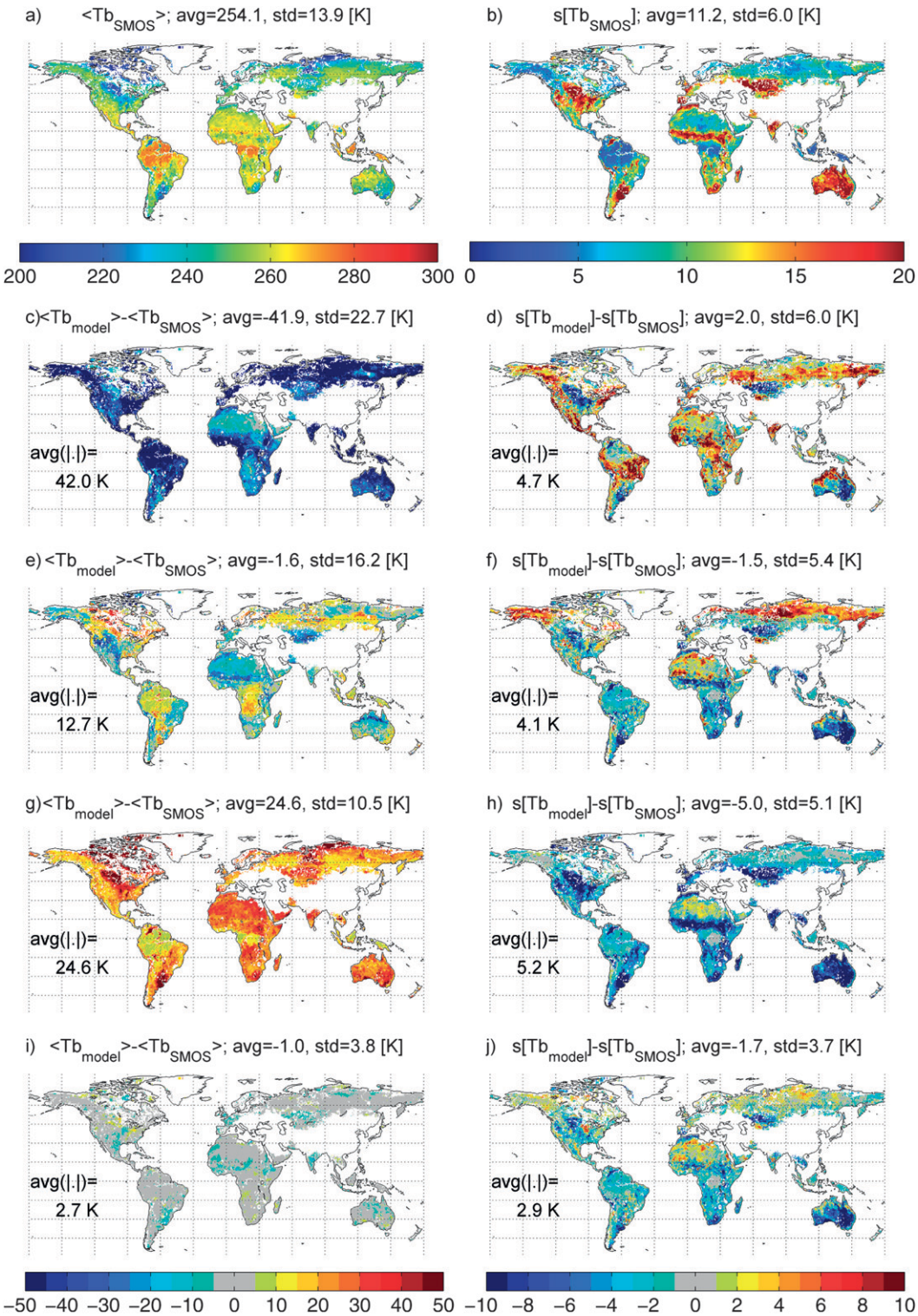


FIG. 2. Time series (a) mean and (b) standard deviation of SMOS $Tb_H(42.5°)$ during the validation period (1 Jul 2010 to 1 Jul 2011), including both ascending and descending orbits. Remaining subplots show the difference of the (left) mean and (right) standard deviation statistics between model simulations and SMOS observations for (c),(d) Lit1; (e),(f) Lit2; (g),(h) Lit3; and (i),(j) CalD2. Within each subplot, titles indicate the global average (avg) and standard deviation (std) across each map. For (c)–(j), the average absolute difference [avg(|·|)] across the map is also indicated.

deviation, indicating consistent simulations and observations across the calibration and validation years. Figures 2c–h also show the differences between Lit1, Lit2, and Lit3 Tb simulations and SMOS observations during the validation period. The global averages of the temporal mean differences (biases) in $Tb_H(42.5°)$ for the validation year are −41.9 K, −1.6 K, and 24.6 K for the Lit1, Lit2, and Lit3 simulations, respectively. For Lit2 the global average bias is lowest, but local biases are still very high; the spatial standard deviation of the bias map is 16.2 K and the average absolute bias is 12.7 K. In densely vegetated areas (e.g., Amazon forest, eastern United States, boreal areas), the Lit2 Tb is typically too warm, whereas the Sahara Desert and the western States are too cold. For Lit1 and Lit3, all locations on the globe are too cold or too warm, respectively. In Lit1, the low vegetation opacity (low LEWT and $b_p$), together with the high rough surface reflectivity (due to low $h$ values), causes colder Tb predictions. Similarly, in Lit3, the higher vegetation opacity and lower reflectivity result in warmer Tb.

The difference between the time series standard deviation of the simulated $Tb_H(42.5°)$ and that of SMOS is 2.0 K, −1.5 K, and −5.0 K for Lit1, Lit2, and Lit3, respectively. Lit3 underestimates the temporal variability because of the large $h$ values, whereas Lit1 and Lit2 have smaller global average biases in temporal variability (with opposite signs) but considerable spatial variations. The average absolute differences are between 4.1 K and 5.2 K for Lit1, Lit2, and Lit3. All three experiments underestimate the SMOS variability in the central United States, southern Australia, and southeastern South America and overestimate it in the Sahara.

### 2) AFTER CALIBRATION

Figures 1 and 2 also show the Tb results during the validation period after calibration for scenario CalD2, that is, simultaneously calibrating $h_{\min}$, $\Delta h$, $b_H$, $\Delta b$, and $\omega$, with prior constraint Lit2. Figure 1 shows that after calibration the angular signature of the simulated Tb matches that of SMOS very well. Figure 2i illustrates that through calibration the long-term mean bias in $Tb_H(42.5°)$ is considerably reduced and now below 5 K in most areas with a global average absolute bias of 2.7 K. Furthermore, Fig. 2j demonstrates that the average absolute bias in the time series variability is also smaller on average (2.9 K). That is, the global mean bias can be reduced and, at the same time, the temporal variability indicated by the observations can be maintained.

While the climatological bias is typically reduced to less than 5 K across all angles, residual seasonal Tb biases remain because the calibration cost function is (intentionally) not designed to mitigate errors at time scales of less than 1 year. To illustrate the remaining biases, Fig. 3 shows Hovmöller plots of calibrated (CalD2) simulations minus SMOS observations, averaged over the six angles and for the period of 1 January 2010 to 1 October 2012. The figures show the evolution of the seasonal biases as a function of latitude (averaged over longitude), split up by polarization and orbit direction. Note that the full-polarization SMOS Tb product used here was only intermittently available prior to April 2010. For both polarizations and orbit directions, the residual seasonal biases mostly range between −10 and 10 K, and the seasonal and latitudinal variations of the biases are very similar across the different years.

In the Northern Hemisphere, the simulation-minus-SMOS average for a given latitude is dominated by estimates from North America, because large portions of Europe and Russia are masked out because of RFI contamination (see Fig. 2). The no-data periods (white) correspond to frozen conditions, which are excluded from the analysis (section 2).

A distinct residual cold bias in 2010 and 2011 is obvious in the ascending V-polarized Tb (Fig. 3b) at approximately 50°N, where SMOS $Tb_V$ is persistently warmer than the modeled near-surface soil temperature $T_s$ (in nature, Tb cannot exceed $T_s$; comparison against $T_s$ not shown). Under such conditions, it is impossible to calibrate the RTM meaningfully. This bias does not show up in the descending V polarization and points to the presence of unfiltered RFI in the SMOS observations, probably caused by a radar system used for military defense purposes. Because of the tilt in the SMOS antenna, the defense radar signal is only picked up in the ascending orbit. For the H polarization, the bias could be suppressed by the calibration, because $Tb_H$ is generally lower than $Tb_V$ and is not similarly constrained by $T_s$. This hypothesis is supported by the absence of the cold bias in ascending $Tb_V$ in 2012, when the contaminating signal was switched off (Y. Kerr 2012, personal communication).

A comparison of Figs. 3a and 3c (and of Figs. 3b and 3d) reveals that there is also a residual global average cold bias in the ascending orbits and a warm bias in the descending orbits: the bias is not minimized for each orbit direction separately but simultaneously for ascending and descending orbits (along with both polarizations and all angles). The opposing signs in the biases of the ascending and descending orbits could suggest a diurnal bias in the simulated $T_s$ (Holmes et al. 2012) or a measurement error related to the different position of the spacecraft with respect to the sun in ascending and descending mode.

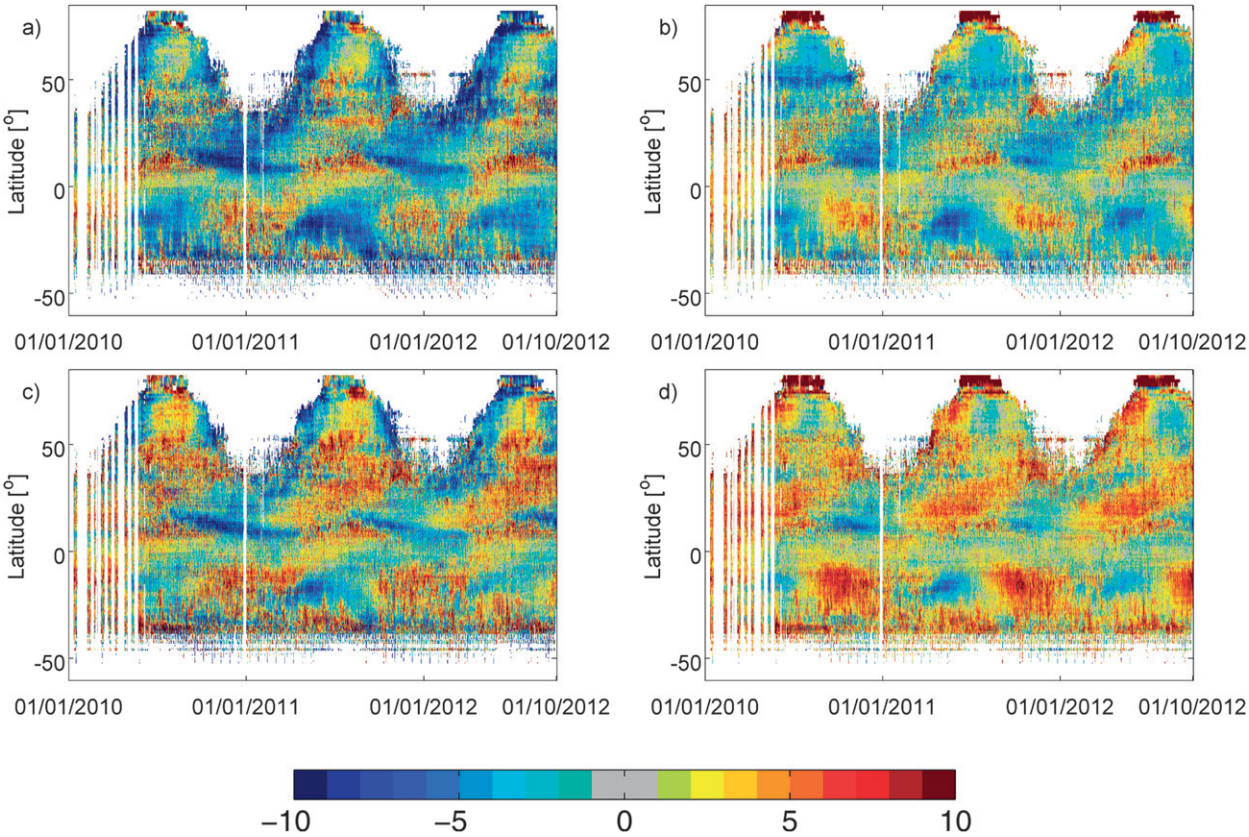


FIG. 3. Hovmöller plots of calibrated (CalD2) minus SMOS Tb (K) for 1 Jan 2010 to 1 Oct 2012, averaged over six incidence angles (32.5°, 37.5°, 42.5°, 47.5°, 52.5°, 57.5°): (a) ascending H polarization, (b) ascending V polarization, (c) descending H polarization, and (d) descending V polarization.

We emphasize again that the short-term errors are not minimized in the calibration. The global root-mean-square difference (RMSD) between the SMOS and the calibrated brightness temperatures remains ~9.5 K for H polarization and ~7.3 K for V polarization (at 42.5° incidence angle and for ascending and descending orbits). These shorter-term biases are caused by model errors such as missed precipitation events, inaccurate vegetation description, etc., or by short-term observation errors and will be addressed through data assimilation.

### b. *Sensitivity of Tb to soil moisture*

The parameter calibration is designed to provide unbiased climatological Tb. Since the calibration of the microwave RTM parameters may unduly increase $h$ to compensate for wet or cold biases in CLSM, it is necessary to check the sensitivity of the modeled Tb to soil moisture after calibration. As a rule of thumb, a 2–3 K increase in Tb is associated with a 0.01 $m^3\ m^{-3}$ decrease in soil moisture for incidence angles around 40° and for low vegetation regions (Jackson 1993; Schmugge and Jackson 1994; Chanzy et al. 1997; Jackson et al. 1999). Figure 4 shows the time–space average change in modeled $Tb_H(42.5°)$ for a 0.01 $m^3\ m^{-3}$ increase in soil moisture for different parameter sets. The values are an annual mean over the full validation year (thus experiencing a range of soil moisture conditions) and averaged over moderate to low vegetation only (IGBP classes CSH, OSH, WSV, SAV, GRS, CRP, and CRN; see Table 1 for definitions). The sensitivity to soil moisture over forested areas is an order of magnitude smaller. Without calibration, the sensitivity for Lit1 is realistic at about −2.5 K $(0.01\ m^3\ m^{-3})^{-1}$, but at the expense of a high bias in Tb (Figs. 1, 2). The average sensitivity for the Lit3 setup is unrealistically low at around −0.3 K $(0.01\ m^3\ m^{-3})^{-1}$, mainly because of the high uniform $h$ = 1.66. Lit2 is again in between Lit1 and Lit3.

During the calibration, the constraint on the temporal Tb variability indirectly imposes a realistic sensitivity of Tb to soil moisture. As a result, all calibrated scenarios show a similar average sensitivity comparable to that of Lit2, ranging from −1.3 to −1.6 K $(0.01\ m^3\ m^{-3})^{-1}$ for H polarization (Fig. 4) and from −0.7 to −1.1 K $(0.01\ m^3\ m^{-3})^{-1}$ for V polarization (not shown) at 42.5°

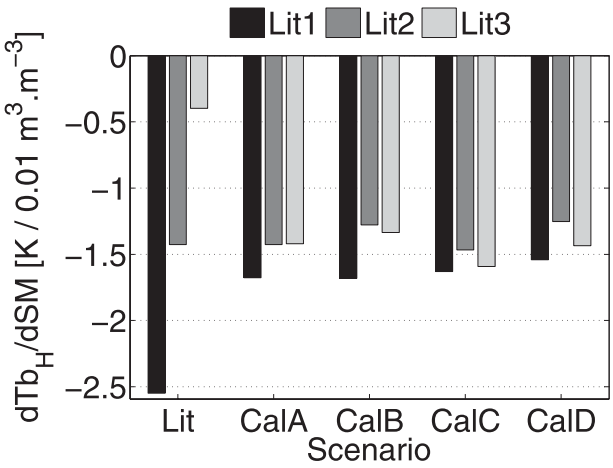


FIG. 4. Sensitivity of ascending $Tb_H(42.5°)$ to soil moisture [(K (0.01 $m^3$ $m^{-3}$)$^{-1}$] before calibration (Lit) and after calibration (CalA, CalB, CalC, CalD), with prior parameter constraints from Lit1, Lit2, and Lit3. The statistics are averaged over nonforested and nondesert areas only (IGBP classes CSH, OSH, WSV, SAV, GRS, CRP, and CRN) during the validation period (1 Jul 2010 to 1 Jul 2011).

incidence angle. Clearly, $h$ has a profound impact on the Tb sensitivity, as shown in the large increase in sensitivity when going from Lit3 to CalA3 (Fig. 4), which both have the same parameters, except for $h$. The relatively higher sensitivity of Tb to soil moisture for calibration scenarios with Lit1 prior constraints is attributed to the relatively lower (prior or calibrated) vegetation opacity $\tau$.

### c. *Calibrated RTM parameter values*

The results in the previous subsection show the modeled and observed Tb. Here, we further analyze the RTM parameter values for the different calibration scenarios. Ultimately, we want to choose a single calibration scenario, with some assurance that the optimal parameters are not too dependent on the calibration setup. For example, we hope to find similar spatial parameter patterns, regardless of the choice of prior constraint values and the selection of calibrated parameters.

#### 1) LOCALLY CALIBRATED PARAMETERS

Given the interaction between the selection of the calibrated and uncalibrated parameters, the different prior value constraints, and the random search during the calibration, it can be expected that each calibration scenario will lead to slightly different sets of calibrated RTM parameters. Figure 5 shows the globally averaged microwave roughness, vegetation opacity, and scattering albedo for each of the three sets of literature values and each of the 12 calibration scenarios. The $h$ and $\tau$

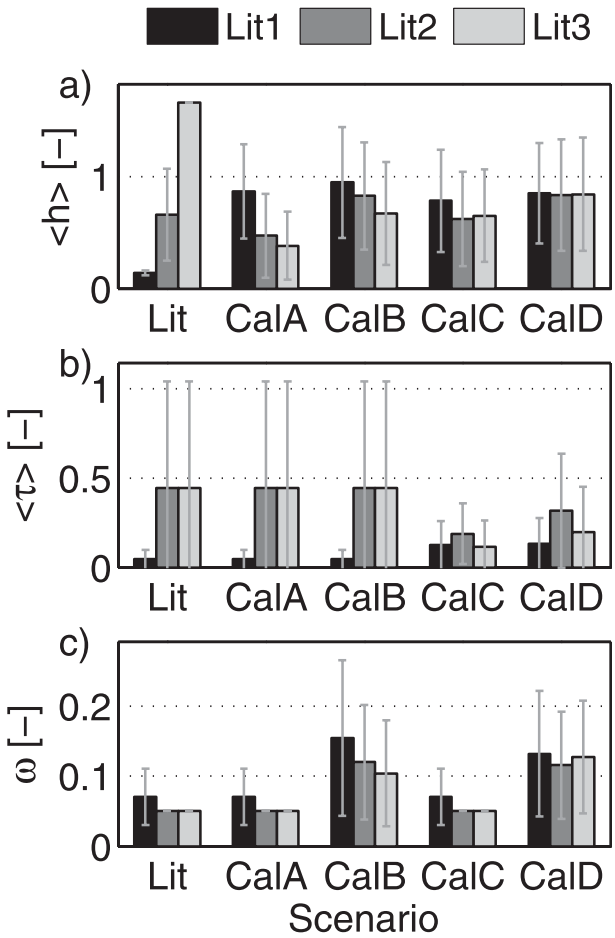


FIG. 5. Globally averaged (a) time-mean $\langle h \rangle$, (b) time-mean $\langle \tau \rangle$, and (c) time-invariant $\omega$ before calibration (Lit) and after calibration (CalA, CalB, CalC, CalD), with prior parameter constraints from Lit1, Lit2, and Lit3. Time-mean values are for the calibration period (1 July 2011 to 1 July 2012).

values are presented as time-mean parameters ($\langle \cdot \rangle$) over the calibration year, because $h$ is diagnosed based on the dynamic soil moisture [Eq. (B1)] and $\tau$ is based on the time-variant LAI [Eq. (5)]. For $\tau$, we present the average of $\tau_H$ and $\tau_V$ because we found them to be similar in magnitude for most vegetation classes. This is not unreasonable for the relatively coarse (43 km) scale of SMOS observations, where vegetation structure effects are averaged for a variety of vegetation types.

To facilitate the interpretation of the results in Fig. 5, bear in mind that a higher $h$, a higher $\tau$, or a lower $\omega$ tend to result in higher Tb values. The calibrated $\langle h \rangle$ values always exceed those of Lit1, because Lit1 mainly reflects the geometric roughness, whereas the calibration is performed for coarse-scale (36 km) heterogeneous pixels. The effective roughness after calibration is therefore

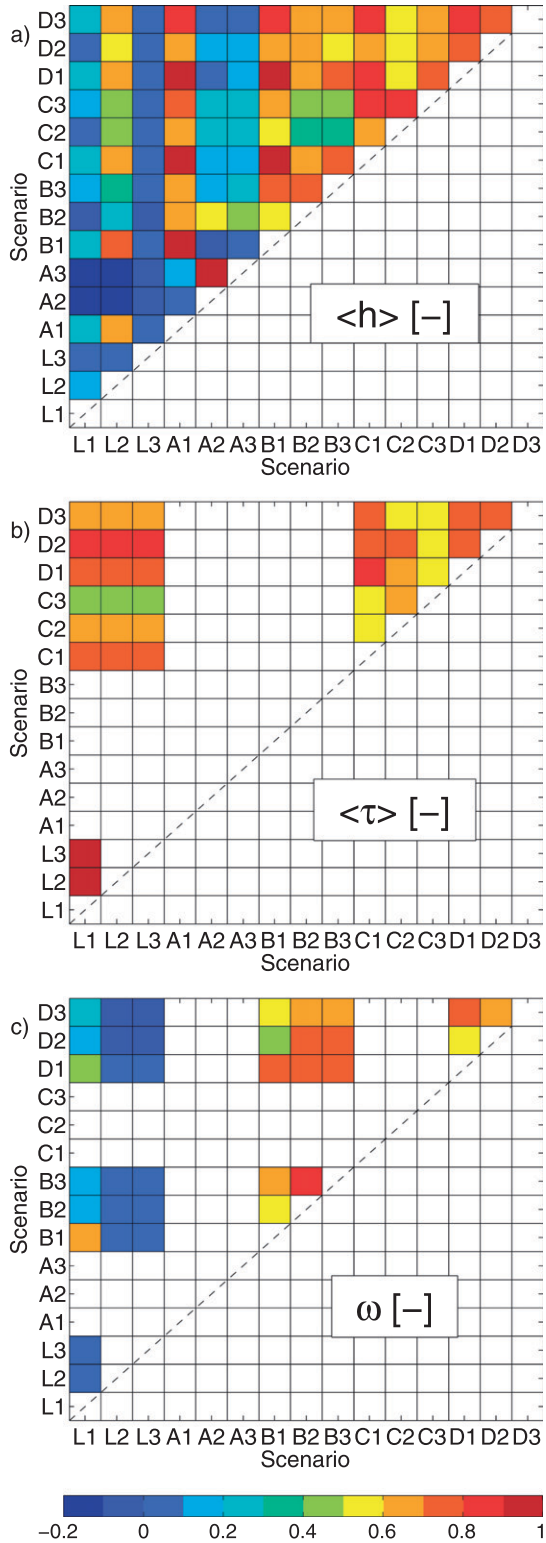


FIG. 6. Spatial correlation between pairs of prior and/or calibrated global parameter fields for (a) time-mean $\langle h \rangle$, (b) time-mean $\langle \tau \rangle$, and (c) time-invariant $\omega$. Trivially perfect correlations (identical prior values) or scenarios where the particular parameter is not calibrated are left blank. Time-mean values are for the calibration period (1 Jul 2011 to 1 Jul 2012).

linked to the SMOS scale and not solely determined by the real dielectric properties that vary at the subwavelength scale. The values of $\langle h \rangle$ are higher when $\tau$ is lower or $\omega$ is higher, which reflects the expected tradeoff between vegetation and soil characteristics in the simulation of Tb. The difference in $\langle h \rangle$ between CalA2 and CalA3 is driven by the difference in $\mathrm{Nr}_p$. In scenario B, $\langle h \rangle$ is slightly higher because $\omega$ is calibrated to higher values. More complexity is added in scenarios C and D where $b_p$ is calibrated [Eq. (5)]. Values of $\tau_p$ appear to be underestimated in Lit1 and are increased through calibration, whereas the calibrated $\tau_p$ values are generally reduced through calibration when Lit2 or Lit3 values are used as prior constraints.

The deviation of the calibrated (effective) parameters from those obtained through calibration of small-scale experimental data (i.e., prior values) may reflect the heterogeneity of the land surface conditions within the low resolution simulation pixels. In addition, uncertainty in the calibrated parameters may originate from inaccuracies in the simulated soil moisture, temperature, and other geophysical fields.

The above assessment of global average values roughly explains the interaction between the parameters, but the optimal parameters exhibit considerable spatial variability as shown by the large spatial standard deviation markers in Fig. 5. Figure 6 shows the global spatial correlation of $\langle h \rangle$ (or $\langle \tau \rangle$ or $\omega$) for values from different literature and calibration scenarios (ignoring scenarios with uncalibrated parameters). The literature values for $\langle h \rangle$ show little mutual spatial correlation (Fig. 6a). However, after calibration, the spatial patterns of $\langle h \rangle$ correlate reasonably well between all calibration scenarios, except for CalA2 and CalA3. In scenario A, all discrepancies between simulated and observed Tb have to be absorbed by $\langle h \rangle$, but the uncalibrated (vegetation) parameters from Lit2 and Lit3 do not allow an optimal $\langle h \rangle$ estimate. When calibrating more parameters in scenarios B, C, and D, the $\langle h \rangle$ patterns become more consistent across calibration scenarios, with spatial correlations generally greater than 0.5.

The spatial patterns of $\langle \tau \rangle$ are quite strongly correlated without calibration because of the LAI signature. The patterns become somewhat less coherent after calibration (C, D), but still agree well. The correlations in $b_p$ (not shown) show positive values between and within calibration scenarios C and D, but zero or negative correlation with the lookup table values. Lastly, $\omega$ also shows a positive correlation (>0.5) between most calibrated scenarios, whereas the resulting pattern is not correlated with any of the prior constraints. In summary, the calibrated parameter values show spatial patterns

that are not overly tied to the prior parameter patterns (based on vegetation classes), and the different calibration scenarios tend toward similar spatial patterns.

2) PREFERRED CALIBRATION SCENARIO (CALD2)

The above analysis suggests that calibration scenario D avoids the situation in which one parameter compensates unrealistically for an uncalibrated and suboptimal parameter. Because the Lit2 prior constraint is in many ways a compromise between Lit1 and Lit3, and because of the slightly lower bias after calibration (see section 4d), we select CalD2 as the preferred scenario. The downside of CalD2 compared to the other CalD scenarios is the relatively lower sensitivity of Tb to soil moisture (Fig. 4) and higher bias in standard deviation (see Fig. 9). This is caused by uncalibrated positive $Nr_p$ values, which effectively decrease the rough surface reflectivity, increase Tb, and decrease its variability.

Figure 7 shows literature and calibrated (CalD2) values for $\langle h \rangle$, $\langle \tau \rangle$, and $\omega$, binned by vegetation class. The calibrated $\langle h \rangle$ values are generally higher for forested areas (IGBP classes ENF, EBF, DNF, ENF, and MXF) and similar to the values suggested in Lit2. The higher values may be related to the typically uneven terrain underlying these less cultivated areas. The higher $\langle h \rangle$ may also compensate for a wet bias in CLSM soil moisture, which may be because there are errors in CLSM soil parameters or because the SMOS-observed signal is affected by a drier litter layer that is not simulated by CLSM. For shorter vegetation, the calibrated $\langle h \rangle$ values are somewhat higher than for Lit2, which agrees with Panciera et al. (2009a) and Sabater et al. (2011), who suggested that the default $h$ values in L-MEB (cf. Lit2) are low for areas with limited vegetation. The calibrated $\tau$ values distinguish between higher and lower vegetation, more so than for Lit1, but less strongly than for Lit2 and Lit3 (Fig. 7). The effective albedo $\omega$ assumes values in the range provided in Lit1 for forests, but for low vegetation classes, an increased $\omega$ is found that effectively reduces the contribution of vegetation to Tb.

For reference, Table 3 lists the corresponding averages and spatial standard deviations of the calibrated (CalD2) values for the parameters $h_{\min}$, $h_{\max}$, $b_H$, and $b_V$ that are underlying the diagnosed $\langle h \rangle$ and $\langle \tau \rangle$ values (Fig. 7), as well as the calibrated $\omega$. It is important to note that the calibrated $b_p$ parameter depends on the source of LAI data and the preset LEWT values. The $b_p$-parameter will also compensate for water in branches, which is not necessarily a linear function of LAI. Furthermore, interception is not taken into account. In a separate experiment (not shown) we found that the calibrated $b_p$ values are slightly lower when interception water is added to the VWC. The difference between $h_{\min}$ and $h_{\max}$ is substantial, which corroborates the dependency of $h$ on soil moisture [Eq. (B1)]. However, the dependency may also result from a mismatch between the actual soil depth contributing to the emission measured by SMOS and the assumed constant soil depth contributing to the simulated Tb (Escorihuela et al. 2010).

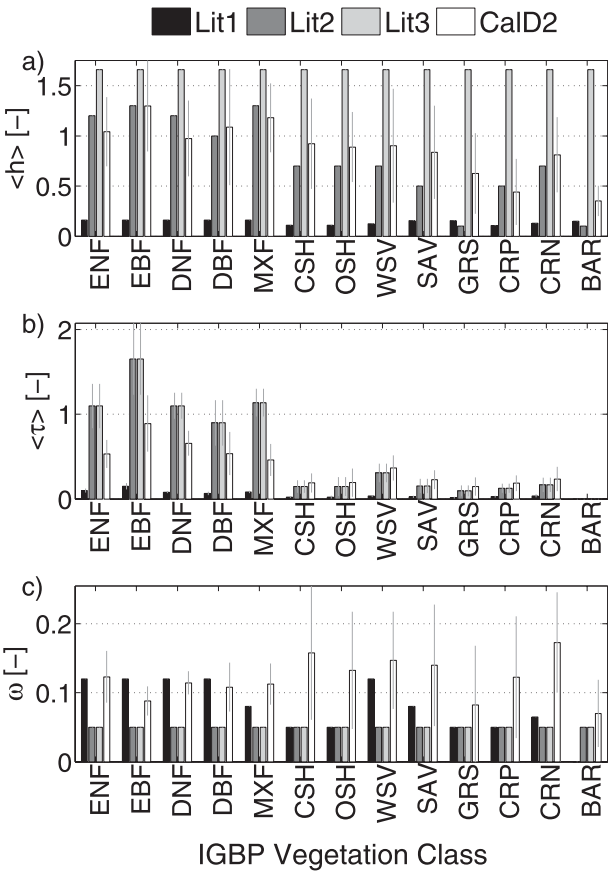


FIG. 7. (a) Time-mean $\langle h \rangle$, (b) time-mean $\langle \tau \rangle$, and (c) time-invariant $\omega$ before calibration (Lit1, Lit2, Lit3) and after calibration (CalD2), spatially averaged by vegetation class. Thin gray lines extending above the bars indicate the spatial standard deviation within each vegetation class. Time-mean values are for the calibration period (1 Jul 2011 to 1 Jul 2012).

Finally, Fig. 8 illustrates $\tau$ retrievals from SMOS and estimates from CalD2 for two watersheds in the United States with different vegetation characteristics. The calibrated $\tau$ values roughly match the magnitude of the retrieved values. However, the retrievals are typically very noisy, whereas the calibrated $\tau$ shows a more realistic, smoother seasonal pattern. It should be recognized that the simulated $\langle \tau \rangle$ is based on a climatological LAI, that is, the calibrated $\tau$ values lack interannual

TABLE 3. Average and spatial standard deviation of calibrated (CalD2) RTM parameters for each IGBP vegetation class.

| IGBP | Class average | | | | | Standard deviation | | | | |
|---|---|---|---|---|---|---|---|---|---|---|
| | $h_{\min}$ | $h_{\max}$ | $\omega$ | $b_H$ | $b_V$ | $h_{\min}$ | $h_{\max}$ | $\omega$ | $b_H$ | $b_V$ |
| 1 ENF | 0.81 | 1.12 | 0.12 | 0.19 | 0.14 | 0.39 | 0.39 | 0.04 | 0.06 | 0.06 |
| 2 EBF | 1.13 | 1.48 | 0.09 | 0.20 | 0.18 | 0.46 | 0.49 | 0.02 | 0.09 | 0.10 |
| 3 ENF | 0.74 | 1.00 | 0.11 | 0.24 | 0.16 | 0.39 | 0.40 | 0.02 | 0.05 | 0.05 |
| 4 DBF | 0.87 | 1.14 | 0.11 | 0.22 | 0.19 | 0.55 | 0.62 | 0.04 | 0.09 | 0.10 |
| 5 MXF | 0.93 | 1.26 | 0.11 | 0.16 | 0.10 | 0.38 | 0.39 | 0.03 | 0.06 | 0.06 |
| 6 CSH | 0.66 | 0.93 | 0.16 | 0.41 | 0.38 | 0.45 | 0.45 | 0.10 | 0.16 | 0.17 |
| 7 OSH | 0.68 | 0.92 | 0.13 | 0.38 | 0.37 | 0.37 | 0.37 | 0.08 | 0.18 | 0.19 |
| 8 WSV | 0.63 | 0.95 | 0.15 | 0.39 | 0.35 | 0.53 | 0.59 | 0.07 | 0.12 | 0.15 |
| 9 SAV | 0.47 | 0.89 | 0.14 | 0.34 | 0.31 | 0.42 | 0.49 | 0.09 | 0.12 | 0.15 |
| 10 GRS | 0.35 | 0.65 | 0.08 | 0.32 | 0.31 | 0.34 | 0.42 | 0.09 | 0.19 | 0.21 |
| 12 CRP | 0.19 | 0.49 | 0.12 | 0.23 | 0.24 | 0.25 | 0.38 | 0.09 | 0.13 | 0.13 |
| 14 CRN | 0.48 | 0.94 | 0.17 | 0.21 | 0.21 | 0.40 | 0.46 | 0.07 | 0.12 | 0.10 |
| 16 BAR | 0.20 | 0.35 | 0.07 | 0.08 | 0.08 | 0.18 | 0.15 | 0.05 | 0.09 | 0.10 |

variability by design. At continental scales, the calibrated RTM parameters show realistic spatial patterns that reflect the general vegetation classification, but the patterns differ from the uniform values for each vegetation class that would be obtained from typical lookup table values (not shown).

#### 3) AGGREGATE PARAMETERS

Although in the previous subsection we presented the calibrated parameters by vegetation class, we again emphasize that the local calibration minimizes the bias at each grid cell individually and that average parameter values for a vegetation class are not necessarily optimal for all locations within that class. When we apply the forward RTM with such aggregated parameter values based on CalD2, the global average biases are smaller than for the uncalibrated Lit1, Lit2, and Lit3. However, the local biases increase substantially compared to what is obtained with local CalD2 parameters. For example, the global average absolute bias for the validation period is 7.1 K when aggregated CalD2 parameters are used, compared to 2.7 K for local CalD2 parameters [$\mathrm{Tb}_H(42.5°)$, Fig. 2i]. In a separate calibration exercise, we optimized the RTM parameters per vegetation class, that is, with an additional sum in $J_{\langle\cdot\rangle,o}$ and $J_{s[\cdot],o}$ [Eq. (6)] to include all grid cells within one vegetation class. In all other respects, this separate calibration was identical to CalD2. With the resulting parameters, the global average absolute bias in ascending $\mathrm{Tb}_H(42.5°)$ is 6.9 K, and the bias pattern is very similar to what is obtained when we use parameters that are aggregated by vegetation class (after local calibration).

Taken together, these results indicate that locations within the same vegetation class, but with different soil classes or in different climate zones, may require different RTM parameters. Furthermore, climatological land cover maps do not necessarily represent the actual local vegetation conditions, and the effective parameters may compensate for unresolved spatial heterogeneity in vegetation. Nevertheless, parameters that have been aggregated by vegetation class (after local calibration) could serve as good initial estimates in regions where reliable SMOS observations are not available for local calibration (because of RFI contamination), while SMAP observations may become available for data assimilation.

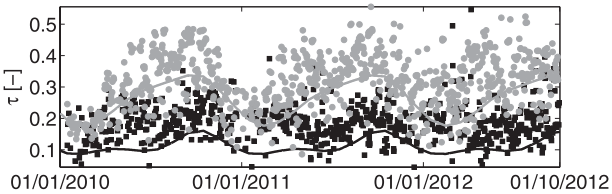


FIG. 8. Time series of SMOS-retrieved (symbols) and Cal2D (lines) vegetation opacity $\tau$, for the Walnut Gulch CalVal watershed in Arizona (black) and the Little River CalVal watershed in Georgia (gray).

### d. Calibration performance

In this subsection we analyze the components of the objective function and the convergence of the optimization. Figure 9 shows the global average total objective function $J$ along with its individual components before and after calibration; $J_{\langle\cdot\rangle,o}$ and $J_{s[\cdot],o}$ are the first and second terms in Eq. (6) and represents the weighted mean square difference between the climatological mean values and standard deviations, respectively. For all scenarios, the largest component of $J$ is $J_{\langle\cdot\rangle,o}$, followed by $J_{s[\cdot],o}$. The smallest contribution is made by the parameter constraint $J_\alpha$. The spatial variability of the $J$ components is large (not shown), especially for the Lit and A scenarios. Through calibration of $h_{\min}$ and $\Delta h$ alone (CalA), a considerable variability in the biases across the globe persists. When more parameters are calibrated (CalB, CalC, and CalD), the $J_o$ components and their spatial variability are reduced further, most so for $J_{\langle\cdot\rangle,o}$; $J_{s[\cdot],o}$ is less reduced, because the temporal variability in the Tb simulations is mostly determined by the land surface conditions, while the RTM parameters have only a second-order effect on the temporal standard deviation in simulated Tb. Furthermore, adjusting the parameters to limit the bias in the mean is not always optimal for controlling the bias in the standard deviation. The reduction in $J_{s[\cdot],o}$ is thus compromised by the reduction in $J_{\langle\cdot\rangle,o}$ (e.g., an increase in $h$ causes warmer Tb with a reduced temporal variability). As

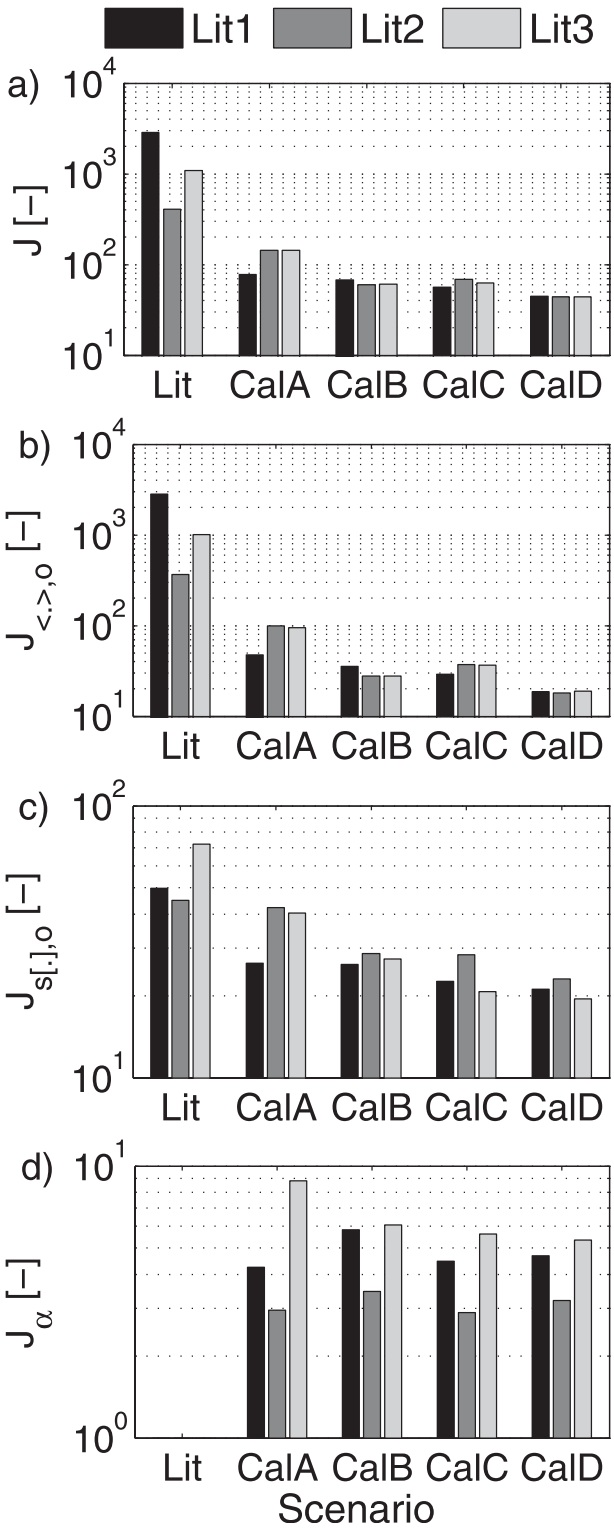


FIG. 9. Globally averaged objective function (a) $J$ and (b)–(d) its components [Eq. (6)] before calibration (Lit) and after calibration (CalA, CalB, CalC, CalD), with prior parameter constraints from Lit1, Lit2, and Lit3. Note the different limits on the vertical axes.

expected, the parameter penalty $J_\alpha$ is always smallest, with Lit2 as prior constraints.

Next, we analyze the convergence of the optimization algorithm to assess the effectiveness of the PSO algorithm in finding the optimal parameter values. Convergence could reflect the closeness of the swarm's best position to the optimum (accuracy) or the contraction of the initial swarm (some measure of precision). There is no reason why precision and accuracy would occur together, that is, a swarm could contract around a local optimum, or a swarm may be spread all over the search space with only a single particle reaching an optimum value (Pedersen and Chipperfield 2010). Here we roughly approximate the convergence by calculating the "ensemble" spread (standard deviation) (i) across the 25 swarm particles when reaching the optimum or (ii) across the three optimal particles, obtained from three repetitions. These measures for ensemble spread could be interpreted as ad hoc estimates of the parameter uncertainty, which depend on the choice of PSO parameters (section 3). An independent parameter uncertainty assessment using Bayesian techniques (e.g., Vrugt et al. 2009) is beyond the scope of this paper and will be addressed in future research.

Figure 10 shows the global average of the prior and posterior ensemble parameter spread for three parameters calibrated in CalD2. The dashed horizontal line is the prior parameter spread, which is based on Table 2, and equal for all grid cells. The black bars show the final spread per vegetation class after the particle swarm has contracted during the iterations (within one PSO repetition). The swarm contracts to half its prior spread for $h_{\min}$ in low vegetation areas and for $\omega$ in high vegetation areas. Interestingly, this exactly reflects the importance of each parameter in more and less vegetated areas, that is, the soil roughness is arguably more important in areas with less vegetation and scattering mainly applies to the vegetation portion in Eq. (1). The spread for $b_H$ also reduces, by up to half of the prior swarm spread. The $\Delta h$ and $\Delta b$ parameters keep a large swarm spread, which highlights their relatively limited importance, that is, slightly different values for $\Delta h$ or $\Delta b$ could yield equally good results in terms of Tb biases (not shown).

The same conclusions hold for the convergence measured by the spread in the three repetitions (white bars in Fig. 10). Note that by analyzing the global average we mitigate the limitation of having only three repetitions. The spread across the optimal parameters is always smaller than the spread across the swarm, because of the limited amount of repetitions and the tendency to pull the optimal parameter for each repetition into the same subsearch space. The limited sample size also causes a larger spatial uncertainty (gray lines) on

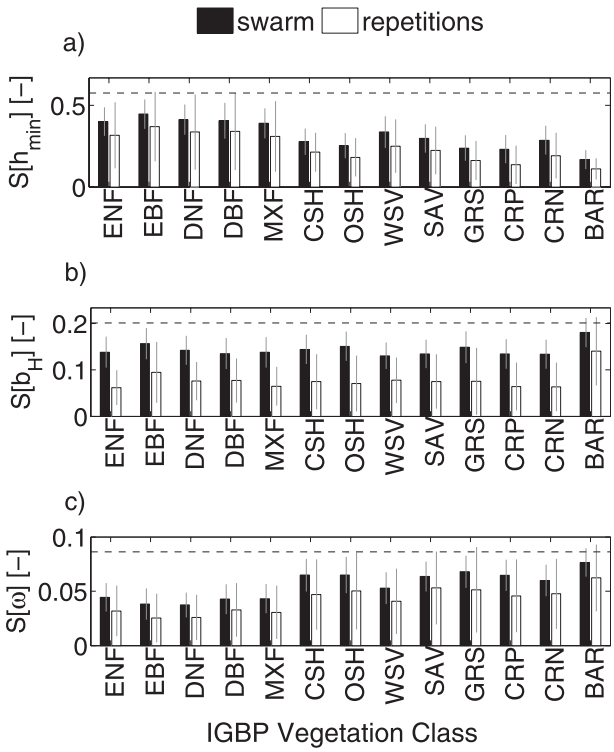


FIG. 10. Measures of convergence for (a) $h_{\min}$, (b) $b_H$, and (c) $\omega$, calibrated with CalD2. The dashed line shows the prior assumed parameter uncertainty. The posterior parameter uncertainty is shown in averages (bars) $\pm 1$ spatial standard deviation (gray vertical lines) per vegetation class. The ensemble standard deviation [$S(\cdot)$] is calculated across the swarm at the end of the PSO iterations (black) and the three optimal values obtained from three repetitions (white).

the uncertainty estimates. We also find that for calibration scenarios with fewer parameters (CalA, CalB, CalC; not shown), the spread reduces more strongly than for the D scenarios where five parameters are calibrated simultaneously: with more parameters there are more options to get equally good Tb results (equifinality). In general, the uncertainty estimates in Fig. 10 indicate that the calibrated parameters are not necessarily unique optimal values, and that slightly different combinations of parameter values could result in similarly good results.

## 5. Conclusions

A zero-order (tau-omega) microwave RTM is added to the GEOS-5 CLSM for a global simulation of multiangular Tb at the scale of SMOS observations and under nonfrozen conditions. When contrasting Tb simulations with literature-based RTM parameters against SMOS observations, large climatological biases up to ~50 K are found. The tested microwave RTM parameter sets are: Lit1 proposed for SMAP L2/3 soil moisture products; Lit2 used in earlier L-MEB research; and Lit3, which is the same as Lit2 but with $\mathrm{Nr}_p = 0$ and the roughness $h = 1.66$ as in the ECMWF monitoring for SMOS.

To obtain climatologically unbiased Tb simulations for a radiance-based soil moisture data assimilation system, the RTM parameters are calibrated at each individual location, using the one year (1 July 2011 to 1 July 2012) of observed multiangular SMOS Tb. During the calibration, we minimize the difference in the climatological mean values and standard deviations between simulations and SMOS observations at different incidence angles and both polarizations. The constraint on the temporal variability indirectly assures a realistic sensitivity of Tb to soil moisture conditions. An additional parameter penalty term in the objective function regularizes the calibration problem. After calibration, the climatological biases are largely removed [e.g., the global average absolute bias is 2.7 K for $\mathrm{Tb}_H(42.5°)$] for all incidence angles. The latter is expected to also hold true on average for the nonsampled incidence angles, because the near-linear shape of the angular signature observed in the SMOS data has inherently been imposed onto the simulations after calibration. Residual biases remain, because of seasonal, diurnal, or persistent model and observation errors, such as, for example, inaccurately simulated soil moisture or unfiltered RFI.

A number of different calibration scenarios are explored, with different parameters selected for calibration and different prior constraints (Lit1, Lit2, and Lit3). Simulations with the prior parameters reveal underestimated roughness $h$ in Lit1 and overestimated roughness for Lit3. When only $h$ is calibrated, the biases are strongly reduced, but suboptimal parameter estimates are found, because of compensation for the uncalibrated vegetation opacity $\tau$ and scattering albedo $\omega$. Inclusion of these latter parameters in the calibration yields more optimal parameter sets that result in the lowest global average Tb biases. However, the parameter convergence is slightly reduced when more parameters are calibrated.

The spatial patterns of the locally calibrated RTM parameters are more realistic than the values corresponding to typical lookup tables, and the resulting spatial variability in the parameters facilitates lower local biases. When the RTM is used with calibrated parameters that are averaged by vegetation classes, the global Tb biases remain small, but local Tb biases increase [e.g., the global average absolute bias is 7.1 K for $\mathrm{Tb}_H(42.5°)$].

It is important to note that the calibrated parameters depend on the specific land surface conditions simulated by the GEOS-5 system. These effective parameters deviate from parameters that have been determined in field experiments or from parameter calibration at small scales, probably because of unresolved heterogeneity in the coarse-scale simulations. Furthermore, calibration of

RTM parameters may compensate for local climatological biases in simulated soil moisture, surface temperature, and vegetation characteristics. A change in any of these factors would require a recalibration of the system. Likewise, a change in any module of the RTM itself, such as, for example, for the dielectric constant, may require a recalibration in order to keep the Tb simulations unbiased. Nevertheless, the calibration of the microwave RTM parameters is a necessary prerequisite for the successful application of the modeling system to the assimilation of L-band Tb from SMOS and SMAP.

The calibrated RTM for GEOS-5 is an essential part of the prototype assimilation system for the generation of the SMAP L4_SM product. As the SMOS data record increases through time, the RTM parameters will be locally recalibrated to fill remaining gaps across the globe. In the future, the calibration will be conducted at the finer 9-km model resolution to facilitate the 9-km SMAP L4_SM analysis product. In areas with insufficient SMOS data to calibrate the RTM parameters locally, vegetation class–averaged parameters will be used as an initial guess. The use of SMOS observations in this approach therefore facilitates the assimilation of SMAP observations as soon as they become available.

*Acknowledgments.* Gabriëlle De Lannoy was a research fellow of the Research Foundation Flanders (FWO). Funding for Gabriëlle De Lannoy and Rolf Reichle was also provided by the NASA Soil Moisture Active Passive mission and by the NASA program on the Science of *Terra* and *Aqua* (NNH09ZDA001N-TERRAQUA). Computing was supported by the NASA High End Computing Program. The first author thanks Niko Verhoest for supporting research abroad. The authors thank Yann Kerr, Patricia de Rosnay, Delphine Leroux, and Ali Mahmoodi for many helpful discussions in the development of this research and Jean-Pierre Wigneron for feedback to this manuscript. We also greatly appreciate the insightful suggestions from three anonymous reviewers.

## APPENDIX A

### Soil Moisture Evaluation

This section provides a brief comparison of CLSM and SMOS soil moisture estimates and a validation against in situ observations. Figure A1 shows the mean difference (MD), unbiased RMSD (ubRMSD; that is, the RMSD after removing the mean difference), and correlation coefficient ($R$) between SMOS and CLSM soil moisture estimates averaged by vegetation class. The global average mean difference is 0.07 $m^3\ m^{-3}$, with the model being wetter than SMOS. This bias comes from both the model and SMOS retrievals: the latter may be slightly dry, as suggested by initial validation studies (Al Bitar et al. 2012; Collow et al. 2012; Lacava et al. 2012), and the model is likely too wet. The ubRMSD is also ~0.07 $m^3\ m^{-3}$ across the globe. Note that these statistics only include observed pixels that passed quality control: for example, only half of the forested area on the globe is included. Higher correlations are found in low vegetation areas. The correlation is high across the United States and negative in the high northern latitudes (not shown). Low correlations between retrievals and simulations are also found in forested areas and in the African desert, where errors in the retrievals are generally larger (de Jeu et al. 2008). The low correlations between SMOS and GEOS-5 may also be due to a lower quality of model precipitation forcings over some of these areas.

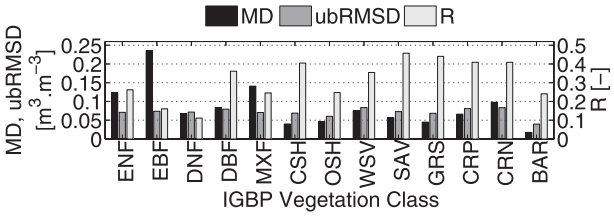


FIG. A1. Evaluation of GEOS-5 vs SMOS soil moisture: MD, ubRMSD, and $R$ for both ascending and descending orbits during 1 Jan 2010 to 1 Oct 2012. Statistics are computed at each grid cell and then averaged by vegetation class.

Further analysis of the CLSM estimates and SMOS retrievals against ground measurements from four U.S. Department of Agriculture Agricultural Research Service watersheds (Jackson et al. 2010) for the year 2010 is summarized in Table A1. These four "CalVal" watersheds include Reynolds Creek (Idaho), Walnut Gulch (Arizona), Little Washita (Oklahoma), and Little River (Georgia). The sensor networks in these areas measure surface soil moisture at the spatially

TABLE A1. Correlation $R$ (–) with 95% confidence interval, bias ($m^3\ m^{-3}$; SMOS or model minus CalVal), and unbiased RMSE [ubRMSE ($m^3\ m^{-3}$)] for SMOS-retrieved and model-simulated soil moisture vs CalVal watershed-averaged observations for the year 2010.

| | | $R$ | Bias | ubRMSE |
|---|---|---|---|---|
| Reynolds Creek | SMOS | 0.61 ±0.09 | −0.018 | 0.048 |
| | Model | 0.68 ±0.08 | 0.073 | 0.040 |
| Walnut Gulch | SMOS | 0.72 ±0.06 | 0.013 | 0.043 |
| | Model | 0.87 ±0.03 | 0.058 | 0.016 |
| Little Washita | SMOS | 0.75 ±0.05 | 0.013 | 0.047 |
| | Model | 0.80 ±0.04 | 0.026 | 0.033 |
| Little River | SMOS | 0.50 ±0.09 | 0.080 | 0.061 |
| | Model | 0.51 ±0.09 | 0.098 | 0.045 |

distributed watershed scale of model and satellite estimates and have been verified in extensive field campaigns, thereby limiting the usual scale discrepancies and other shortcomings of comparisons between model estimates or satellite retrievals versus measurements from in situ sensor networks (Jackson et al. 2010; Liu et al. 2011). The SMOS observations correlate well ($R > 0.7$) with in situ observations at Walnut Gulch and Little Washita. Slightly lower correlations are found for Reynolds Creek and Little River ($R = 0.61 \pm 0.09$ and $0.50 \pm 0.09$). The performance for CLSM in terms of correlation is best at Walnut Gulch ($R = 0.87 \pm 0.03$) and comparable to that of SMOS for the remaining three watersheds. The bias in the SMOS observations is always smaller than in the CLSM simulations. In general, CLSM overestimates soil moisture by 0.05 $m^3\ m^{-3}$ or more for various reasons: for example, at Walnut Gulch the CLSM estimates do not account for surface rocks and therefore appear much wetter than the in situ measurements that have been corrected for rocks (Cosh et al. 2008).

## APPENDIX B

### RTM Parameterization

Table 1 summarizes the Lit1, Lit2, and Lit3 values of the microwave RTM parameters. The parameters that determine the soil contribution to Tb are $h$ and $\mathrm{Nr}_p$. The values for the microwave soil roughness $h$ differ greatly across the three sets of literature values. The lower $h$ values of Lit1 reflect an interpretation of roughness as actual surface height variations (commonly known as geometric roughness). In contrast, the higher $h$ values of Lit3 reflect an effective roughness that accounts for spatial soil moisture heterogeneity and volume scattering (Mo and Schmugge 1987; Wigneron et al. 2001; Merlin et al. 2009). The Lit3 value is calculated as $h = (2k\sigma)^2 = 1.66$ (Choudhury et al. 1979), where $\sigma$ (cm) is the standard deviation of the surface roughness equal to 2.2 cm (Sabater et al. 2011) and $k = 2\pi/\lambda$ ($\mathrm{cm}^{-1}$) is the wavenumber, with $\lambda$ the wavelength (cm). The $h$ values for Lit2 are mainly based on Wigneron et al. (2007) and range between Lit1 and Lit3.

A multitude of physically based and semiempirical schemes suggest that $h$ depends on soil moisture, incidence angle, and the model choice for the soil dielectric constant (Wigneron et al. 2001; de Jeu et al. 2009; Panciera et al. 2009b; Sabater et al. 2011; Escorihuela et al. 2010). For the parameter calibration, we include the reported dependence of $h$ on soil moisture [SM ($m^3\ m^{-3}$)] through a stepwise linear expression [adapted from the proposed SMOS soil moisture retrieval algorithm (CESBIO et al. 2011; Kerr et al. 2012)]:

$$h = \begin{cases} h_{\max} & \text{if} \quad \mathrm{SM} \le \mathrm{wt} \\ h_{\max} + \dfrac{h_{\min} - h_{\max}}{\mathrm{poros} - \mathrm{wt}}(\mathrm{SM} - \mathrm{wt}) & \text{if} \quad \mathrm{wt} < \mathrm{SM} \le \mathrm{poros} \end{cases}, \tag{B1}$$

where poros ($m^3\ m^{-3}$) and wt ($m^3\ m^{-3}$) are the porosity and transition soil moisture, respectively. The latter is modeled as wt = 0.48wp + 0.165 (Wang and Schmugge 1980) where wp ($m^3\ m^{-3}$) is the wilting point; $h_{\min}$ is the value of $h$ for soil moisture at saturation, whereas $h_{\max}$ is the value of $h$ for soil moisture at or below the transition soil moisture. In Lit1, Lit2, and Lit3, $h$ does not depend on soil moisture, that is, $h = h_{\min} = h_{\max}$. The exponent $\mathrm{Nr}_p$ is uniformly set to 0 for both Lit1 and Lit3 (Mo and Schmugge 1987; Wigneron et al. 2001). However, polarization-dependent values have been suggested in more recent studies (Escorihuela et al. 2007; Wigneron et al. 2007; Grant et al. 2007; Panciera et al. 2009a; Sabater et al. 2011) and are included in the Lit2 parameter set. Note that the currently operational SMOS retrieval algorithm uses a similar linear piecewise relationship between $h$ and soil moisture [Eq. (B1)] for nominal surfaces (low vegetation and bare soil) using $h_{\min} = 0.05$, $h_{\max} = 0.1$, and an additional transition point at the field capacity beyond which $h = h_{\max}$. For water bodies, wetland, urban areas, and ice, $h$ is uniformly set to 0. For forests and barren areas, $h$ is uniformly set to 0.3.

As shown in Eq. (5), we use LAI and LEWT to characterize the vegetation opacity. The LEWT values for Lit1 shown in Table 1 are based on Yilmaz et al. (2008, and references therein) for different vegetation types. Note that the SMAP Level 2 passive soil moisture products use the Normalized Difference Vegetation Index (NDVI) to parameterize $\tau$ rather than the LAI, so LEWT values for Lit1 were not taken from O'Neill et al. (2012). A typical value for vegetation types other than forests is LEWT = 0.5 kg $m^{-2}$ (Wigneron et al. 2002; Drusch et al. 2009), which is used in Lit2 and Lit3. For forests we formally set LEWT = 1 kg $m^{-2}$. The vegetation structure parameter $b_p$ depends not only on the vegetation type and stage, but also on the polarization, wavelength (Jackson and Schmugge 1991), and incidence angle (van de Griend and Wigneron 2004). In Table 1, we assign time- and

angle-independent $b_p$ values for L band based on Jackson and O'Neill (1990), Jackson and Schmugge (1991), and Crow et al. (2005) for Lit1. For Lit2 and Lit3, $b$ values are based on Pellarin et al. (2003) and de Rosnay et al. (2009). For the calibration, $b_p$ depends on the polarization.

The last vegetation-dependent parameter, the scattering albedo $\omega_p$, typically ranges between 0.05 and 0.12, but Jackson and O'Neill (1990) and Jackson and Schmugge (1991) use $\omega_p = 0.0$, whereas van de Griend et al. (1996) also found higher values for L band. Here we assign a polarization- and angle-independent $\omega$. In Lit1, $\omega$ depends on vegetation type (Crow et al. 2005), whereas a uniform $\omega = 0.05$ is used in Lit2 and Lit3 (Drusch et al. 2009; de Rosnay et al. 2009) (Table 1).

## REFERENCES


Al Bitar, A., D. Leroux, Y. H. Kerr, O. Merlin, P. Richaume, A. Sahoo, and E. F. Wood, 2012: Evaluation of SMOS soil moisture products over continental U.S. using the SCAN/SNOTEL network. *IEEE Trans. Geosci. Remote Sens.,* **50,** 1572–1586.

Balsamo, G., J.-F. Mahfouf, S. Bélair, and G. Deblonde, 2006: A global root-zone soil moisture analysis using simulated L-band brightness temperature in preparation for the Hydros satellite mission. *J. Hydrometeor.,* **7,** 1126–1146.

Bircher, S., J. E. Balling, N. Skou, and Y. H. Kerr, 2012: Validation of SMOS brightness temperatures during the HOBE airborne campaign, western Denmark. *IEEE Trans. Geosci. Remote Sens.,* **50,** 1468–1482.

Campbell, G., 1974: A simple method for determining unsaturated conductivity from moisture retention data. *Soil Sci.,* **117,** 311–314.

CESBIO, IPSL, INRA, Reading University, and Tor Vergata University, cited 2011: Algorithm Theoretical Basis Document (ATBD) for the SMOS Level 2 Soil Moisture Processor Development Continuation Project, Issue 3.4, 121 pp. [Available online at http://www.cesbio.ups-tlse.fr/data_all/SMOS-doc/atbd/ATBD_v3_4_20110124.pdf.]

Chanzy, A., S. Raju, and J. Wigneron, 1997: Estimation of soil microwave effective temperature at L and C bands. *IEEE Trans. Geosci. Remote Sens.,* **35,** 570–580.

Choudhury, B. J., T. J. Schmugge, A. Chang, and R. W. Newton, 1979: Effect of surface roughness on the microwave emission from soils. *J. Geophys. Res.,* **84** (C9), 5699–5706.

Collow, T. W., A. Robock, J. B. Basara, and B. G. Illston, 2012: Evaluation of SMOS retrievals of soil moisture over the central United States with currently available in situ observations. *J. Geophys. Res.,* **117,** D09113, doi:10.1029/2011JD017095.

Cosh, M. H., T. J. Jackson, S. Moran, and R. Bindlish, 2008: Temporal persistence and stability of surface soil moisture in a semi-arid watershed. *Remote Sens. Environ.,* **112,** 304–313.

Crow, W. T., and Coauthors, 2005: An observing system simulation experiment for Hydros radiometer-only soil moisture products. *IEEE Trans. Geosci. Remote Sens.,* **43,** 1289–1303.

de Jeu, R. A. M., W. Wagner, T. R. H. Holmes, A. J. Dolman, N. van de Griesen, and J. Friesen, 2008: Global soil moisture patterns observed by space borne microwave radiometers and scatterometers. *Surv. Geophys.,* **29,** 399–420.

——, T. R. H. Holmes, R. Panciera, and J. P. Walker, 2009: Parameterization of the land parameter retrieval model for L-band observations using the NAFE'05 data set. *IEEE Geosci. Remote Sens. Lett.,* **6,** 630–634.

De Lannoy, G., R. Reichle, P. Houser, V. Pauwels, and N. Verhoest, 2007: Correcting for forecast bias in soil moisture assimilation with the ensemble Kalman filter. *Water Resour. Res.,* **43,** W09410, doi:10.1029/2006WR005449.

de Rosnay, P., and Coauthors, 2006: SMOSREX: A long term field campaign experiment for soil moisture and land surface processes remote sensing. *Remote Sens. Environ.,* **102,** 377–389, doi:10.1016/j.rse.2006.02.021.

——, and Coauthors, 2009: AMMA land surface model intercomparison experiment coupled to the Community Microwave Emission Model: ALMIP-MEM. *J. Geophys. Res.,* **114,** D05108, doi:10.1029/2008JD010724.

Dobson, M., F. Ulaby, M. Hallikainen, and M. A. El-Rayes, 1985: Microwave dielectric behavior of wet soil—Part II: Dielectric mixing models. *IEEE Trans. Geosci. Remote Sens.,* **23,** 35–46.

Drusch, M., E. F. Wood, and T. J. Jackson, 2001: Vegetation and atmospheric corrections for the soil moisture retrieval from passive microwave remote sensing data: Results from the Southern Great Plains Hydrology Experiment 1997. *J. Hydrometeor.,* **2,** 186–192.

——, T. Holmes, P. de Rosnay, and G. Balsamo, 2009: Comparing ERA-40-based L-band brightness temperatures with Skylab observations: A calibration/validation study using the Community Microwave Emission Model. *J. Hydrometeor.,* **10,** 213–226.

Entekhabi, D., and Coauthors, 2010: The Soil Moisture Active and Passive (SMAP) mission. *Proc. IEEE,* **98,** 704–716.

Escorihuela, M. J., T. H. Kerr, P. de Rosnay, J. Wigneron, J. Calvet, and F. Lemaitre, 2007: A simple model of the bare soil microwave emission at L-band. *IEEE Trans. Geosci. Remote Sens.,* **45,** 1978–1987.

——, A. Chanzy, J. Wigneron, and Y. Kerr, 2010: Effective soil moisture sampling depth of L-band radiometry: A case study. *Remote Sens. Environ.,* **114,** 995–1001.

Ferrazzoli, P., L. Guerriero, S. Paloscia, and P. Pampaloni, 1995: Potential of multifrequency techniques in microwave radiometry of crops. *Microwave Radiometry and Remote Sensing of the Environment,* D. Solimini, Ed., VSP, 391–400.

Fitzmaurice, J. A., and W. Crow, 2011: Online vegetation parameter estimation using passive microwave observations for soil moisture estimation. Preprints, *25th Conf. on Hydrology,* Seattle, WA, Amer. Meteor. Soc., 49. [Available online at https://ams.confex.com/ams/91Annual/webprogram/Paper185647.html.]

Grant, J., J. Wigneron, A. A. Van de Griend, A. Kruszewski, S. S. Sobjaerg, and N. Skou, 2007: A field experiment on microwave forest radiometry: L-band signal behaviour for varying conditions of surface wetness. *IEEE Trans. Geosci. Remote Sens.,* **109,** 10–19.

——, K. Saleh-Contell, J. Wigneron, M. Guglielmetti, Y. H. Kerr, M. Schwank, S. Skou, and A. A. Van de Griend, 2008: Calibration of the L-MEB model over a coniferous and deciduous forest. *IEEE Trans. Geosci. Remote Sens.,* **46,** 808–818.

Holmes, T. R. H., M. Drusch, J. P. Wigneron, and R. A. M. D. Jeu, 2008: A global simulation of microwave emission: Error structures based on output from ECMWF's operational integrated forecast system. *IEEE Trans. Geosci. Remote Sens.,* **46,** 846–856.

——, T. J. Jackson, R. H. Reichle, and J. B. Basara, 2012: An assessment of surface soil temperature products from

numerical weather prediction models using ground-based measurements. *Water Resour. Res.,* **48,** W02531, doi:10.1029/2011WR010538.

Jackson, T. J., 1993: Measuring surface soil moisture using passive microwave remote sensing. *Hydrol. Processes,* **7,** 139–152.

——, and P. O'Neill, 1990: Attenuation of soil microwave emissivity by corn and soybeans at 1.4 and 5 GHz. *IEEE Trans. Geosci. Remote Sens.,* **28,** 978–980.

——, and T. J. Schmugge, 1991: Vegetation effects on the microwave emission of soils. *Remote Sens. Environ.,* **36,** 203–212.

——, D. M. L. Vine, A. Y. Hsu, A. Oldak, P. J. Starks, C. T. Swift, J. D. Isham, and M. Haken, 1999: Soil moisture mapping at regional scales using microwave radiometry: The southern Great Plains hydrology experiment. *IEEE Trans. Geosci. Remote Sens.,* **37,** 2136–2151.

——, and Coauthors, 2010: Validation of advanced microwave scanning radiometer soil moisture products. *IEEE Trans. Geosci. Remote Sens.,* **48,** 4256–4272.

Kennedy, J., and R. Eberhart, 1995: Particle swarm optimization. *Proc. IEEE Int. Conf. on Neural Networks,* Vol. 4, Piscataway, NJ, IEEE, 1942–1948.

Kerr, Y. H., and E. G. Njoku, 1990: A semiempirical model for interpreting microwave emission from semiarid land surfaces as seen from space. *IEEE Trans. Geosci. Remote Sens.,* **28,** 384–393.

——, and Coauthors, 2010: The SMOS mission: New tool for monitoring key elements of the global water cycle. *Proc. IEEE,* **98,** 666–687.

——, and Coauthors, 2012: The SMOS soil moisture retrieval algorithm. *IEEE Trans. Geosci. Remote Sens.,* **50,** 1384–1403.

Koster, R. D., M. J. Suarez, A. Ducharne, M. Stieglitz, and P. Kumar, 2000: A catchment-based approach to modeling land surface processes in a general circulation model 1. Model structure. *J. Geophys. Res.,* **105** (D20), 24 809–24 822.

Kurum, M., P. O'Neill, R. Lang, A. Joseph, M. Cosh, and T. Jackson, 2012: Effective tree scattering and opacity at L-band. *Remote Sens. Environ.,* **118,** 1–9.

Lacava, T., P. Matgen, L. Brocca, M. Bittelli, N. Pergola, T. Moramarco, and V. Tramutoli, 2012: A first assessment of the SMOS soil moisture product with in situ and modeled data in Italy and Luxembourg. *IEEE Trans. Geosci. Remote Sens.,* **50,** 1612–1622.

Le Vine, D., G. S. E. Lagerloef, F. R. Colomb, S. H. Yueh, and F. A. Pellerano, 2007: An instrument to monitor sea surface salinity from space. *IEEE Trans. Geosci. Remote Sens.,* **45,** 2040–2050.

Liu, Q., R. Reichle, R. Bindlish, M. Cosh, W. C. R. de Jeu, G. De Lannoy, G. Huffman, and T. Jackson, 2011: The contribution of precipitation forcing and satellite observations of soil moisture on the skill of soil moisture estimates in a land data assimilation system. *J. Hydrometeor.,* **12,** 750–765.

Martín-Neira, M., and Coauthors, 2012: SMOS instrument performance and calibration. *Proc. IEEE Int. Geoscience and Remote Sensing Symp.,* Munich, Germany, IEEE, WE1.10.1.

Merlin, O., J. P. Walker, R. Panciera, M. J. Escorihuela, and T. J. Jackson, 2009: Assessing the SMOS soil moisture retrieval parameters with high-resolution NAFE'06 data. *IEEE Geosci. Remote Sens. Lett.,* **6,** 635–639.

Mironov, V., M. Dobson, V. Kaupp, S. Komarov, and V. Kleshchenko, 2004: Generalized refractive mixing dielectric model for moist soil. *IEEE Trans. Geosci. Remote Sens.,* **42,** 773–785.

Mo, T., and T. J. Schmugge, 1987: A parameterization of the effect of surface roughness on microwave emission. *IEEE Trans. Geosci. Remote Sens.,* **25,** 47–54.

Montzka, C., and Coauthors, 2013: Brightness temperature and soil moisture validation at different scales during the SMOS validation campaign in the Rur and Erft catchments, Germany. *IEEE Trans. Geosci. Remote Sens.,* **51,** 1728–1743.

O'Neill, P., E. Njoku, T. Jackson, S. Chan, and R. Bindlish, 2012: SMAP Algorithm Theoretical Basis Document (ATBD): SMAP Level 2 &3 soil moisture (passive). Tech. Rep. SMAP Project JPL D-66481, Jet Propulsion Laboratory, Pasadena, CA, 75 pp. [Available online at http://smap.jpl.nasa.gov/files/smap2/L2&3_SM_P_InitRel_v1_filt2.pdf.]

Owe, M., R. de Jeu, and T. Holmes, 2008: Multi-sensor historical climatology of satellite-derived global land surface moisture. *J. Geophys. Res.,* **113,** F01002, doi:10.1029/2007JF000769.

Pan, M., A. Sahoo, W. Wood, A. Al Bitar, D. Leroux, and Y. Kerr, 2012: An initial assessment of SMOS derived soil moisture over the continental United States. *IEEE J. Sel. Top. Earth Obs. Remote Sens.,* **5,** 1448–1457.

Panciera, R., J. P. Walker, J. D. Kalma, E. J. Kim, K. Saleh, and J.-P. Wigneron, 2009a: Evaluation of the SMOS L-MEB passive microwave soil moisture retrieval algorithm. *Remote Sens. Environ.,* **13,** 435–444.

——, ——, and O. Merlin, 2009b: Improved understanding of soil surface roughness parameterization for L-band passive microwave soil moisture retrieval. *IEEE Trans. Geosci. Remote Sens.,* **6,** 625–629.

Pauwels, V. R. N., and G. J. M. De Lannoy, 2012: Multivariate calibration of a water and energy balance model in the spectral domain. *Water Resour. Res.,* **47,** W07523, doi:10.1029/2010WR010292.

Pedersen, M. E. H., and A. Chipperfield, 2010: Simplifying particle swarm optimization. *Appl. Soft Comput.,* **10,** 618–628.

Pellarin, T., and Coauthors, 2003: Two-year global simulation of L-band brightness temperatures over land. *IEEE Trans. Geosci. Remote Sens.,* **42,** 2135–2139.

Reichle, R. H., 2012: The MERRA-land data product (version 1.2). GMAO Office Note 3, 43 pp. [Available online at http://gmao.gsfc.nasa.gov/pubs/docs/Reichle541.pdf.]

——, D. B. McLaughlin, and D. Entekhabi, 2001: Variational data assimilation of microwave radio brightness observations for land surface hydrology applications. *IEEE Trans. Geosci. Remote Sens.,* **39,** 1708–1718.

——, S. V. Kumar, S. P. P. Mahanama, R. D. Koster, and Q. Liu, 2010: Assimilation of satellite-derived skin temperature observations into land surface models. *J. Hydrometeor.,* **11,** 1103–1122.

——, R. D. Koster, G. J. M. De Lannoy, B. A. Forman, Q. Liu, S. P. P. Mahanama, and A. Toure, 2011: Assessment and enhancement of MERRA land surface hydrology estimates. *J. Climate,* **24,** 6322–6338.

——, W. Crow, R. Koster, J. Kimball, and G. De Lannoy, 2012: SMAP Algorithm Theoretical Basis Document (ATBD): SMAP L4 surface and root zone soil moisture (L4_SM) data product. Tech. Rep. SMAP Project JPL D-66483, Jet Propulsion Laboratory, Pasadena, CA, 78 pp. [Available online at http://smap.jpl.nasa.gov/files/smap2/L4_SM_InitRel_v1.pdf.]

Rienecker, M. M., and Coauthors, 2011: MERRA: NASA's Modern-Era Retrospective Analysis for Research and Applications. *J. Climate,* **24,** 3624–3648.

Sabater, J. M., P. de Rosnay, and G. Balsamo, 2011: Sensitivity of L-band NWP forward modelling to soil roughness. *Int. J. Remote Sens.,* **32,** 5607–5620, doi:10.1080/01431161.2010.507260.

Saleh, K., J.-P. Wigneron, P. de Rosnay, J.-C. Calvet, M. J. Scorihuela, Y. Kerr, and P. Waldteufel, 2006: Impact of rain interception by

vegetation and mulch on the L-band emission of natural grass. *Remote Sens. Environ.,* **101,** 127–139.

——, ——, P. Waldteufel, P. de Rosnay, M. Schwank, J.-C. Calvet, and Y. Kerr, 2007: Estimates of surface soil moisture under grass covers using L-band radiometry. *Remote Sens. Environ.,* **109,** 42–53.

Scheerlinck, K., V. R. N. Pauwels, H. Vernieuwe, and B. De Baets, 2009: Calibration of a water and energy balance model: Recursive parameter estimation versus particle swarm. *Water Resour. Res.,* **45,** W10422, doi:10.1029/2009WR008051.

Schmugge, T., and T. J. Jackson, 1994: Mapping surface soil moisture with microwave radiometers. *Meteor. Atmos. Phys.,* **54,** 213–223.

Trelea, I., 2003: The particle swarm optimization algorithm: Convergence analysis and parameter selection. *Inf. Process. Lett.,* **85,** 317–325.

van de Griend, A. A., and J. Wigneron, 2004: The b-factor as a function of frequency and canopy type at H-polarization. *IEEE Trans. Geosci. Remote Sens.,* **42,** 786–794.

——, M. Owe, J. de Ruiter, and B. Gouweleeuw, 1996: Measurement and behavior of the dual-polarization vegetation optical depth and single scattering albedo at 1.4- and 5-GHz microwave frequencies. *IEEE Trans. Geosci. Remote Sens.,* **34,** 957–965.

Vrugt, J. A., C. ter Braak, C. Diks, B. A. Robinson, J. M. Hyman, and D. Higdon, 2009: Accelerating Markov chain Monte Carlo simulation by differential evolution with self-adaptive randomized subspace sampling. *Int. J. Nonlinear Sci. Numer. Simul.,* **10,** 271–288.

Wang, J. R., and T. J. Schmugge, 1980: An empirical model for the complex dielectric permittivity of soils as a function of water content. *IEEE Trans. Geosci. Remote Sens.,* **18,** 288–295.

——, and B. J. Choudhury, 1981: Remote sensing of soil moisture content over bare field at 1.4 GHz frequency. *J. Geophys. Res.,* **86,** 5277–5282.

Wigneron, J.-P., J.-C. Calvet, A. Chanzy, and Y. H. Kerr, 1993: Microwave emission of vegetation: Sensitivity to leaf characteristics. *IEEE Trans. Geosci. Remote Sens.,* **31,** 716–725.

——, L. Laguerre, and Y. H. Kerr, 2001: A simple parameterization of the L-band microwave emission from rough agricultural soils. *IEEE Trans. Geosci. Remote Sens.,* **39,** 1697–1707.

——, A. Chanzy, J.-C. Calvet, A. Olioso, and Y. H. Kerr, 2002: Modelling approaches to assimilating L band passive microwave observations over land surfaces. *J. Geophys. Res.,* **107,** 4219, doi:10.1029/2001JD000958.

——, and Coauthors, 2007: L-band microwave emission of the biosphere (L-MEB) model: Description and calibration against experimental data sets over crop fields. *Remote Sens. Environ.,* **107,** 639–655.

Wösten, J. H. M., Ya. A. Pachesky, and W. J. Rawls, 2001: Pedotransfer functions: Bridging the gap between available basic soil data and missing soil hydraulic characteristics. *J. Hydrol.,* **251,** 123–150.

Yilmaz, M. T., E. R. Hunt, and T. J. Jackson, 2008: Remote sensing of vegetation water content from equivalent water thickness using satellite imagery. *Remote Sens. Environ.,* **112,** 2514–2522.

Zhang, S., J. Shi, and Y. Dou, 2012: A soil moisture assimilation scheme based on the microwave Land Emissivity Model and the Community Land Model. *Int. J. Remote Sens.,* **33,** 2770–2797.